Atomistic Simulation of Polymer Melt Elasticity: Calculation of the Free Energy of an Oriented Polymer Melt

Vlasis G. Mavrantzas and Doros N. Theodorou*

Department of Chemical Engineering, University of Patras, and, Institute of Chemical Engineering and High Temperature Chemical Processes, GR 26500 Patras, Greece

Received October 9, 1997; Revised Manuscript Received April 24, 1998

ABSTRACT: A method is developed for predicting the elasticity of a polymer melt through detailed atomistic simulations. The Helmholtz energy of a melt oriented by flow is postulated to be of the form $A(T,\rho,\tilde{\mathbf{c}})$, where T is the temperature, ρ is the mass density, and $\tilde{\mathbf{c}}$, the conformation tensor, is defined as the end-to-end tensor reduced by one-third the mean squared unperturbed end-to-end distance and averaged over all chains. The conjugate thermodynamic variable to $\tilde{\mathbf{c}}$, $\boldsymbol{\alpha}$, is a tensorial orienting field intimately related to the strain rate in a flow situation. Assuming affine deformation of chain ends, the stress tensor $\boldsymbol{\tau}$ can be expressed in terms of $\tilde{\mathbf{c}}$ and $\boldsymbol{\alpha}$. We have mapped out $\tilde{\mathbf{c}}$, A, and $\boldsymbol{\tau}$ for melts subjected to elongational flow by conducting Monte Carlo (MC) simulations at various values of α_{xx}, all other components of $\boldsymbol{\alpha}$ being zero. Two linear polyethylene melts, of mean chain lengths C_{24} and C_{78} and polydispersity index 1.09, have been studied. Efficient sampling of oriented melt configurations has been made possible through the use of the end-bridging MC algorithm. Comparison of the melt response to that of isolated chains subjected to the same orienting field shows that, while at low fields the two responses are similar, at high fields more anisotropy develops in the melt due to favorable lateral interactions between the oriented chains. Comparison against simple models used in flow calculations shows that FENE dumbbells and freely-jointed chains are more representative of the actual melt response than Hookean dumbbells, because they account for the finite extensibility of the polymer. Partitioning A into its energetic and entropic components shows that the melt response is purely entropic for long chains and low orienting fields, which leave the intrinsic shape of chains (averaged in the coordinate frame of their principal axes) practically unaltered. A significant energetic contribution develops for small chains and high orienting fields, where the chain intrinsic shape becomes more elongated and attractive lateral interchain interactions are intensified. Values of $\boldsymbol{\tau}$ calculated from $\tilde{\mathbf{c}}$ and $\boldsymbol{\alpha}$ are consistent with virial theorem predictions.

1. Introduction

In their majority, atomistic modeling investigations of polymer systems with molecular dynamics (MD) and Monte Carlo (MC) techniques[1−4] have focused on equilibrium physical properties (e.g., density as a function of temperature and pressure, cohesive energy density, solubility of gases in the melt, gas−liquid phase equilibria in oligomeric systems) and on short-time dynamics (rates of segmental reorientation and torsional transitions, diffusivities of small penetrant molecules in melts). Special molecular mechanics (MM) and transition-state theory (TST) based techniques have been developed to address the small-deformation mechanical response of configurationally arrested glassy systems,[5,6] small-molecule diffusion[7,8] and side-group relaxational motions[9] in such systems. However, in real-life polymer processing operations one is also interested in a set of very important long-time dynamic and viscoelastic properties (such as the stress relaxation modulus, the zero-shear rate viscosity, and the storage and loss moduli), which primarily govern the rheological behavior and processability of the polymer in the melt state. A relatively small number of equilibrium and nonequilibrium MD simulations relevant to these properties, employing atomistic or coarse-grained continuum models, have appeared recently.[10−14] Generally, however, progress in relating melt rheological properties to the detailed molecular-level characteristics of chains has been slow. Although statistical mechanics offers a rigorous formalism for calculating such properties from molecular geometry and atomic interactions, its numerical implementation, through simulations, to polymers has faced a number of important challenges, prominent among which has been the tremendous breadth of time- and length-scale spectra that govern structure and molecular motion in these systems. As an example, the relaxation time of the end-to-end vector of chains in a melt can exceed by orders of magnitude the maximum time spans (typically tens of nanoseconds) that can be simulated today with reasonable computational resources. This is true even for an unentangled polymer melt; the mere equilibration of a linear polyethylene melt of molecular weight around 2000 is impossible by conventional MD techniques.

The macroscopic continuum mechanical modeling and simulation (e.g., by finite element methods) of polymer flows has had a long and successful history. Typically, such modeling employs simple constitutive equations, whose form or parameters cannot be directly related to the molecular characteristics of chains.[15−17] On the other hand, there are polymer models, incorporating more molecular detail, such as the reptation model of Doi and Edwards[18] and the phase-space theory of Curtiss and Bird,[19,20] which may be intractable by traditional continuum mechanical methods, either due to the impossibility of being cast as a closed-form constitutive equation or due to the extreme complexity of such an equation.[20] Promising stochastic simulation

* Author to whom correspondence should be addressed at the University of Patras. Phone: +3061-997-398. Fax: +3061-993-255. E-mail: doros@sequoia.chemeng.upatras.gr.

S0024-9297(97)01487-3 CCC: $15.00
Published on Web 08/15/1998

techniques have been developed[21] for dealing with such models in specific flow situations. Still, however, there is much need to connect the parameters invoked by these more "molecular" models to the chemical constitution and architecture of chains or to refine the models further so that they provide a better representation of reality. Today, the polymer industry faces serious difficulties when trying to predict the processing behavior of polymer melts from their molecular constitution or to design polymers with tailored processing characteristics; melt fracture phenomena observed during extrusion or film blowing of high density, low density, linear low density, and metallocene polyethylenes exemplify this.[22]

Clearly, hierarchical approaches are needed to bridge the huge gap in time and length scales between motion of polymer segments and flow in melt processing equipment. The work discussed here is part of a more general, cooperative effort aimed at developing a molecular-based approach to the modeling of polymer processing flow operations, which will involve three interconnected levels. The first (most fundamental) level provides the link to the detailed chemical constitution of the polymeric fluid of interest; it involves atomistic simulations. The second is the mesoscopic level, wherein a coarse-grained picture of the polymeric fluid is invoked through the use of a number of global descriptors for the overall polymer structure and their evolution in a stress field. The third is the macroscopic level: this considers the behavior of the fluid under actual processing conditions and aims at producing results for immediate application in industrial operations. Through the analysis at the atomistic level, which we begin to discuss in the present paper, we expect to extract, from chemical constitution, parameters widely invoked at the mesoscopic level. These include a free energy function (involving appropriate "entropy springs") to describe melt elasticity, a monomer friction coefficient, and the entanglement spacing.

This paper focuses on the prediction of melt elasticity. Key to the simulation approach proposed is a new, powerful MC algorithm that enables calculating the free energy of long-chain polymer melts as a function of the overall chain orientation. This Monte Carlo algorithm is based on the end-bridging move, which was introduced for the first time by Pant and Theodorou,[23] to provide vigorous sampling of configuration space by inducing large changes in the conformations of polymer chains in a dense medium. Of course, the MC algorithm cannot generate dynamic trajectories; in fact, its efficiency stems from its ability to overcome free energy barriers that limit the configurational rearrangement of real melts. Nevertheless, it can give rigorous estimates of thermodynamic properties and also provide ensembles of realistic configurations for subsequent dynamic studies.

Oriented polymer melts have been sampled in the past in the course of nonequilibrium molecular dynamics (NEMD) simulations of shear flow.[14] These simulations have employed very high shear rates $\dot{\gamma}$ ($\geq 10^{10}$ s^{-1}) in order to stay within the limits of the available computational time. Such shear rates are well beyond the limits of linear response theory for long polymers; the estimated shear viscosities exhibit a strong dependence on the shear rate (shear-thinning), and their extrapolation by 8−12 orders of magnitude in shear rate to the conditions commonly employed in polymer processing operations is risky. For melts of relatively high molecular weight, the characteristic time of deformations simulated in such NEMD approaches is very short in relation to the longest relaxation time of the melt and comparable to the time scale for transitions of individual torsion angles. Therefore, the internal degrees of freedom of the chains are not given sufficient time to relax according to the imposed field, and the response of the system to the external perturbation is rather glassy than meltlike.

In the present work, problems associated with very large strain rates are avoided. In mapping out the melt free energy as a function of the conformation tensor, which is a global descriptor of long-range conformation, all fast, internal degrees of freedom of all chains present are allowed to equilibrate subject to the considered value of the conformation tensor. In the simulations, at every value of the imposed orienting field, the melt configurations sampled relax completely to an equilibrium strained state; this is made possible within modest computer time by the end-bridging MC method. Ensembles of strained configurations created in this way are excellent starting points for subsequent investigations of dynamic properties (spectrum of relaxation times, zero-shear viscosity, relaxation modulus). One strategy for such investigations involves tracking the evolution of the atomistically detailed configurations upon removal of the orienting field with isothermal−isobaric MD and interpreting the observed decay of the conformation tensor in the light of a coarse-grained dynamical model (Rouse or reptation). Results from such dynamical studies will be reported in future publications.

This paper discusses the Monte Carlo generation of oriented melt configurations and the calculation of their free energy as a function of the degree of chain orientation. The paper is organized as follows: Section 2 reviews recent advances in the theory of polymer melt elasticity. Section 3 develops the thermodynamic and statistical mechanical formulation underlying this work. Section 4 introduces the molecular model used and the concept of continuous unperturbed chains (CUCs) and explains the computational methodology for simulating polymer melt elasticity. Section 5 applies our thermodynamic formulation to limiting cases, corresponding to well-known simple theoretical models for polymer chains. Results from the atomistic simulation work are presented and compared with the response of CUCs and with simple model predictions in section 6. Major conclusions are summarized and discussed in section 7.

2. Theoretical Approaches to Polymer Elasticity

In the classical picture of rubberlike solids, use is made of the idea of chemical or physical cross-links, described as points or junctions at which connecting portions of molecules are forced to move together at all times. In developing the classical molecular theories of rubberlike elasticity, two postulates have been of critical importance.[24] The first states that rubberlike elasticity is an intramolecular property. That is, although intermolecular interactions do unquestionably occur in rubberlike materials, these interactions are independent of configuration. Thus, intermolecular interactions are assumed to be independent of the extent of deformation, and therefore to play no role in deformations carried out at constant volume and composition. The second postulate is closely related to the first and

states that the Helmholtz energy of the elastic network is separable into a liquidlike nonelastic (independent of deformation) and an elastic (dependent on deformation) part:

$$\frac{A}{N} = \frac{A_{\text{liq}}}{N}(T,\rho) + \frac{A_{\text{el}}}{N}(\mathbf{C}) \tag{1}$$

where $\mathbf{C}$ is an appropriately defined strain tensor. In eq 1, A stands for the extensive Helmholtz energy, N is the number of chain molecules, ρ is the mass density, and T is the absolute temperature.

In some of the theories, it is further assumed that the deformation is affine, that is, that the cross-link points move in a geometrically similar way to the macroscopic external boundaries of the elastomeric sample.[25−27] As nicely reviewed in ref 24, this assumption was relaxed in the phantom theory and in the more modern constraint junction and slip-link models. It is also frequently assumed that the chain end-to-end distances follow a Gaussian distribution. This is in general satisfactory, except for chains that are unusually stiff or very short or brought close to the limit of their full extension by the deformation process. These ideas have defined the general framework on which all molecular theories of rubberlike elasticity for macromolecular solids have been based.

Building upon these ideas, intense research since the early years has aimed at extending the theory to study the viscoelastic properties not of rubbers but of polymer melt systems. One can distinguish between two different major paths of thought. The first involves the development of network models for entangled concentrated polymer solutions and polymer melts. The second proceeds by developing free energy-based constitutive equations for unentangled dilute polymer solutions or unentangled polymer melts.

In network models such as the Lodge[28] and the Wagner[29] models, the idea of cross-links is ported to macromolecular fluids by assuming that polymer−polymer interactions are localized at junctions, a junction being a strong local interaction between specific points along two different polymer chains, constraining these points to move together. While in rubbery solids the junctions refer to permanent cross-links, in macromolecular fluids they are viewed as temporary physical entanglements of various complexities and lifetimes. In a melt the junctions are not permanent but are continually being created and destroyed. However, the central idea of rubber elasticity theory is still used in describing polymer−polymer interactions by the temporary cooperative movement of molecular segments joined by these transient cross-links.

In the second path of thought, use is made of irreversible thermodynamics principles together with the introduction of an appropriate number of internal structural parameters describing conformations in a polymer fluid in an overall sense. In a flow situation, these structural parameters (slow dynamical variables) depart from their values in the equilibrium quiescent fluid, while all other (faster) degrees of freedom track the evolution of the structural parameters, i.e., are assumed to be at equilibrium subject to the constraints imposed by the values of the structural parameters at all times. Even if the system depends on variables with intrinsic relaxation times on the order of the time scales of externally imposed changes, it is still possible to describe it accurately enough through an extended fundamental equation of thermodynamics; this may be done provided that the thermodynamic state space is properly extended to include the structural parameters, which account for intermediate microscopic configurations in a nonequilibrium process. Such a structural parameter, which has found wide use in thermodynamic theories of polymer systems, is the conformation tensor, corresponding to the second moment of the distribution function for the polymer end-to-end vector.

Application of these ideas to the dynamic modeling of complex fluids has led to the development of the "Hamiltonian" formulation of continuum mechanics equations using Poisson brackets.[30−32] Building on this last work, Beris and Edwards[33] offered a unified view of transport phenomena (relaxation and diffusion) in dissipative systems based on the idea of the generalized Poisson bracket formalism. When this formalism is used to describe the dynamics of a structureless medium, it correctly reduces to the traditional equations of transport phenomena, i.e., of momentum (Navier−Stokes), heat, and mass transfer. Moreover, in the absence of driving forces for flow it reduces to the requirement of minimal free energy with respect to the structural parameters, in accord with the requirements of equilibrium thermodynamics. The formalism is quite general and can be used efficiently to derive the governing equations describing large deformations within an elastic solid or the relaxation of a viscoelastic fluid. Furthermore, when used in conjunction with a microscopic model for the internal structure, it offers a means for modeling complex interfacial phenomena, such as wall slip of a polymer solution flowing past a (interacting or noninteracting) surface.[34,35]

In generalized Poisson bracket formulations of transport phenomena in viscoelastic liquids, the modeling effort reduces to two, almost independent, steps. In the first, the macroscopic step, the mass, momentum, and energy balance and constitutive equations are developed in terms of the free energy functional of the system. The second is a microscopic step, where the free energy functional is formulated on the basis of consideration of the microscopic physics of the problem. In polymer systems, this second step involves adopting an analytical expression for the part of the free energy that accounts for polymer elasticity. Usually, rather simple forms are used, such as the Gaussian (Hookean dumbbell) model,[33] in which polymer molecules are treated as isolated, noninteracting chains in the spirit of the affine network model of rubber elasticity, with their free energy being a simple function of the invariants of the conformation tensor (compare section 5).

In the next section, the idea of introducing a structural parameter is utilized in developing a free energy function for oriented polymer melts, which can be extracted directly from atomistic simulation.

3. Thermodynamics of an Oriented Polymer Melt

Our objective in this section is to quantify how the free energy of a linear polymer melt depends on the orientational state of the constituent macromolecules. Guided by recent irreversible thermodynamics-based approaches to modeling polymer flows,[33,36] we first define a global descriptor of the polymer melt configuration by the so-called conformation tensor $\tilde{\mathbf{c}}$. We define the conformation tensor as the reduced second moment

tensor of the end-to-end distance vector of a polymer chain, averaged over all chains in the system:

$$\tilde{\mathbf{c}} = 3\left\langle \frac{\mathbf{RR}}{\langle R^2\rangle_0}\right\rangle \tag{2}$$

In eq 2, $\boldsymbol{R}$ stands for the end-to-end vector of a macromolecule and $\langle R^2\rangle_0$ is the mean-squared magnitude of that vector in the unperturbed state. The outer average is taken over all chains in the system under study. In a quiescent (underformed) equilibrium polyethylene melt, chain conformational statistics is unperturbed, to an excellent approximation (Flory random coil hypothesis,[25] confirmed by well-equilibrated atomistic simulations[23]); therefore, $\tilde{\mathbf{c}}$ reduces to the unit tensor $\mathbf{I}$. When the melt is subjected to deformation over time scales shorter than or comparable to the longest relaxation time of the chains, however, the macromolecules will be oriented and $\tilde{\mathbf{c}}$ will depart from its equilibrium isotropic value. In such a case, the six independent components of $\tilde{\mathbf{c}}$ provide a measure of the extension and orientation of the chains along the three axes of the coordinate system.

Having defined $\tilde{\mathbf{c}}$, we postulate that the oriented melt is governed by a Helmholtz energy function A/N, which has a direct dependence on $\tilde{\mathbf{c}}$:

$$\frac{A}{N} = \frac{A}{N}(\rho, T, \tilde{\mathbf{c}}) \tag{3}$$

From the point of view of equilibrium statistical mechanics, the Helmholtz energy function considered in eq 3 is a potential of mean force with respect to the conformation tensor $\tilde{\mathbf{c}}$, defined under the condition that microscopic degrees of freedom sample all configurations consistent with a given value of $\tilde{\mathbf{c}}$ according to the probability density distribution of the canonical ensemble. In other words, all possible configurations that the N-chain system can adopt at a given temperature and density are categorized according to the value of the conformation tensor $\tilde{\mathbf{c}}$. For each category, a partition function is computed. $N\,(A/N)(\rho,T,\tilde{\mathbf{c}})$, an extensive property, is calculated as k_BT times the negative logarithm of this partition function.

With eq 3 having been postulated, the question is how to obtain A/N as a function of $\tilde{\mathbf{c}}$. To this end, it is convenient to consider the conjugate thermodynamic variables to ρ and $\tilde{\mathbf{c}}$, each of which plays the role of a thermodynamic field. The first is a scalar quantity, the field b, defined as

$$b = -\frac{\partial}{\partial(V/N)}\left[\frac{A}{N}(\rho,T,\tilde{\mathbf{c}})\right]_{T,\tilde{\mathbf{c}}} = \rho^2\left[\frac{\partial}{\partial\rho}\frac{A}{N}(\rho,T,\tilde{\mathbf{c}})\right]_{T,\tilde{\mathbf{c}}}\frac{N_A}{M} \tag{4}$$

with V, M, and N_A symbolizing the total volume, number-average molecular weight, and Avogadro's number, respectively. The second is a tensorial quantity, the "orienting field" $\boldsymbol{\alpha}$, defined as

$$\alpha_{\gamma\delta} = \frac{1}{k_BT}\left[\frac{\partial}{\partial\tilde{c}_{\gamma\delta}}\frac{A}{N}(\rho,T,\tilde{\mathbf{c}})\right]_{T,\rho,\tilde{c}[\gamma\delta]} \tag{5}$$

where $\gamma, \delta \in \{1, 2, 3\}$ are indices corresponding to the three coordinate axes and $\tilde{c}_{[\gamma\delta]}$ means that all other components of the tensor $\tilde{\mathbf{c}}$ remain constant except $\tilde{c}_{\gamma\delta}$. Clearly, the tensors $\tilde{\mathbf{c}}$ and $\boldsymbol{\alpha}$ are symmetric; in fundamental equations of the type of eq 3, each tensor can be condensed into a vector of six independent elements, as is done in the thermodynamics of elasticity.[37]

If chain end positions are assumed to transform affinely in a homogeneous deformation field (ref 37, p 9), then the scalar field b and the tensorial quantities $\boldsymbol{\alpha}$ and $\tilde{\mathbf{c}}$ can be related directly to the stress $\boldsymbol{\tau}$ developing in the polymer. To show this, one can start from the general expression for stress given by rational thermodynamics (ref 39, Chapter 4; ref 36). Considering the free energy per unit mass, $(A/N)(N_A/M)$, as a function of temperature T and the deformation gradient tensor[38,39] $\mathbf{F}$, the stress tensor $\boldsymbol{\tau}$ is

$$\boldsymbol{\tau} = \rho\mathbf{F}\cdot\left(\frac{\partial\left(\frac{A}{N}\frac{N_A}{M}\right)}{\partial\mathbf{F}}\right)^{T} \tag{6}$$

Now, if chain ends are taken as the material points representing the polymer in a continuum formulation, and these points are envisioned as undergoing the homogeneous (affine) deformation described by the deformation gradient tensor $\mathbf{F}$, one can readily show (see proof in Appendix A) that

$$\tilde{\mathbf{c}} = \mathbf{F}\cdot\mathbf{F}^{T} \tag{7}$$

The right-hand side of eq 7 can be identified with the Green tensor $\mathbf{B}$ (ref 39, p 81).

As shown in Appendix B, combining eqs 6 and 7 leads to

$$\tau = -b\mathbf{I} + 2\frac{N_A}{M}\rho\tilde{\mathbf{c}}\cdot\left[\frac{\partial\frac{A}{N}(\rho,T,\tilde{\mathbf{c}})}{\partial\tilde{\mathbf{c}}}\right]_{\rho,T,[\tilde{\mathbf{c}}]} = -b\mathbf{I} + 2\frac{N_A}{M}k_BT\rho(\tilde{\mathbf{c}}\cdot\boldsymbol{\alpha}) \tag{8}$$

In other words, the stress tensor in the polymer melt, $\boldsymbol{\tau}$, is obtainable from b, $\boldsymbol{\alpha}$, and $\tilde{\mathbf{c}}$ on purely macroscopic rational thermodynamics grounds, on the assumption of an affine deformation of chain ends. One should note that an expression for the elastic contribution to the stress tensor equivalent to eq 8 has been used extensively in ref 33 (pp 114, 117, 222, 226, 303, 322, 331, 341, and 360) and in the works discussed therein.

In the absence of an orienting field $\boldsymbol{\alpha}$ (i.e., for $\boldsymbol{\alpha} = \mathbf{0}$), eq 8 reduces to $\boldsymbol{\tau} = -b\mathbf{I}$. Therefore, in this special case of a quiescent equilibrium melt, the field b can be identified with the equilibrium pressure P of the system. In general, however, $-3b$ cannot be equated to the trace of the stress tensor, as clearly seen from eq 8.

Strictly, $\boldsymbol{\alpha}$ is a thermodynamic partial derivative. Given an equation describing the evolution of $\boldsymbol{\tau}$ or $\tilde{\mathbf{c}}$ in time, however, it is possible to ascribe a kinematic interpretation to $\boldsymbol{\alpha}$. In a homogeneous flow situation, $\boldsymbol{\alpha}$ is determined by the externally imposed strain rate tensor. The faster the flow in relation to the longest relaxation time of the melt, the higher the value of $\boldsymbol{\alpha}$. Generally, the magnitude of the elements of $\boldsymbol{\alpha}$ is indicative of the Deborah number of the flow. This interpretation becomes exact in the case of the Gaussian chain model subjected to extensional flow (see section 6).

Different forms and time dependences of $\boldsymbol{\alpha}$ can be chosen to simulate specific macroscopic flow situations. The calculations reported in this paper concern melts subjected to homogeneous extensional flow at constant

strain rate in the x-direction. Such a flow is a good approximation of the situation encountered locally in steady-state fiber spinning processes. As shown in section 4, this flow situation corresponds to a constant α_{xx}, all other components of $\boldsymbol{\alpha}$ being zero. Another interesting flow situation is that encountered in the flow relaxation experiment, wherein an initial elongational strain is imposed on the polymer at $t = 0^+$ and kept constant at all times $t > 0$, and the decay of the stress $\boldsymbol{\tau}$ is monitored as a function of time. In this case, the conformation tensor starts off at $\tilde{\mathbf{c}}(0^+) \neq \mathbf{I}$ and decays toward an asymptotic value of $\mathbf{I}$ as time progresses. In this case the field $\boldsymbol{\alpha}(t)$ is time-dependent, its value at every instant being given by eq 5, with $\tilde{\mathbf{c}} = \tilde{\mathbf{c}}(t)$ being the conformation tensor prevailing in the polymer at that instant. The evolution of the stress $\boldsymbol{\tau}(t)$ is obtainable from b, $\tilde{\mathbf{c}}(t)$, and $\boldsymbol{\alpha}(t)$ through eq 8.

A Legendre transformation of the free energy A/N with respect to V/N and $\tilde{\mathbf{c}}$ gives a new thermodynamic potential function,

$$\frac{\tilde{G}}{N} = \frac{\tilde{G}}{N}(b,T,\boldsymbol{\alpha}) = \frac{A}{N} + \frac{b}{\rho}\frac{M}{N_A} - k_B T \boldsymbol{\alpha}:\tilde{\mathbf{c}} \tag{9}$$

with $k_B T \boldsymbol{\alpha}:\tilde{\mathbf{c}}$ accounting for the energy due to the imposed field (field energy). Furthermore,

$$\tilde{c}_{\gamma\delta} = -\frac{1}{k_B T}\left[\frac{\partial}{\partial \alpha_{\gamma\delta}}\frac{\tilde{G}}{N}(b,T,\alpha)\right]_{T,b,\alpha_{[\gamma\delta]}} \tag{10}$$

From the microscopic point of view, the configuration-space probability density corresponding to the fundamental representation, eq 9, is generated by the partition function

$$Q[N,b,T,\boldsymbol{\alpha}] = \text{const}\int \mathrm{d}^{3n}r\, \mathrm{d}V \times \exp\left[-\frac{1}{k_B T}\left(V(\mathbf{r}_1,\mathbf{r}_2,...,\mathbf{r}_n) + bV - k_B T \sum_{i=1}^{N} \boldsymbol{\alpha}:\tilde{\mathbf{c}}_i\right)\right] \tag{11}$$

where $V(\mathbf{r}_1,\mathbf{r}_2,...,\mathbf{r}_n)$ is the potential energy of a given molecular configuration, defined by the position vectors $\mathbf{r}_1, \mathbf{r}_2, ..., \mathbf{r}_n$ of the n interaction sites (mers) comprising the system, and

$$\tilde{\mathbf{c}}_i = 3\frac{\mathbf{R}_i\mathbf{R}_i}{\langle R_i^2\rangle_0} \tag{12}$$

is the conformation tensor of chain i, defined in terms of its end-to-end vector $\mathbf{R}_i$.

Given the relationship between the canonical partition function and the Helmholtz energy, one can readily show[40] that, in the thermodynamic limit,

$$\tilde{G}(N,b,T,\boldsymbol{\alpha}) = -k_B T \ln Q[N,b,T,\boldsymbol{\alpha}] \tag{13}$$

In the simulations to be discussed in the following sections, we will actually be working with melts characterized by a certain degree of polydispersity. The molecular weight distribution in these melts will be controlled by imposing the chemical potentials for different chain lengths. How this can be done has been discussed by Pant and Theodorou.[23] Following that work, we will be considering polymer melts under conditions of fixed total number of chains N, total number of mers n, and relative chemical potentials $\{\mu_k^*\}$ for all chain species (from monomer, $k = 1$, to n-mer, $k = n$) except two ($k = l$, $k = j$), which will be taken as reference species. In addition, the temperature T and the fields b and $\boldsymbol{\alpha}$ will be kept constant. The thermodynamic development of ref 23 carries through to our case, where an orienting field is present. The probability density in the $NnbT\boldsymbol{\mu}^*\boldsymbol{\alpha}$ ensemble considered here is given by

$$\rho^{NnbT\boldsymbol{\mu}^*\boldsymbol{\alpha}}(V,\mathbf{r}_1,...,\mathbf{r}_n;\text{connectivity}) = \text{const}\exp\left[-\frac{1}{k_B T}\left(-\sum_{\substack{k=1\\k\neq l,j}}^{n}\mu_k^* N_k + bV + V(\mathbf{r}_1,\mathbf{r}_2,...,\mathbf{r}_n;\text{connectivity}) - k_B T\sum_{i=1}^{N}\boldsymbol{\alpha}:\tilde{\mathbf{c}}_i\right)\right] \tag{14}$$

In eq 14, N_k stands for the number of chains of length k mers. The index k enumerates different chain species in the system, while the index i runs over all chains present in a configuration. Clearly,

$$\sum_{k=1}^{n} N_k = N \qquad \sum_{k=1}^{n} kN_k = n \tag{15}$$

The probability density of eq 14 is that of the $NnbT\boldsymbol{\mu}^*$ ensemble of Pant and Theodorou,[23] augmented by the factor $\exp[-k_B T\boldsymbol{\alpha}:\sum_{i=1}^{N}\tilde{\mathbf{c}}_i]$, which couples the orienting field $\boldsymbol{\alpha}$ to the conformation tensors of all chains.

From the partition function $Q[N,n,b,T,\boldsymbol{\mu}^*,\boldsymbol{\alpha}]$ (normalizing factor of the probability density of eq 14), one obtains the thermodynamic potential $\tilde{G}(N,n,b,T,\boldsymbol{\mu}^*,\boldsymbol{\alpha})$ through an equation entirely analogous to eq 13. In turn, $\tilde{G}/N$ is related to the Helmholtz energy[23] $A/N(\rho,T,x_1,x_2,...,x_{n-1},\tilde{\mathbf{c}})$ through an equation analogous to eq 9,

$$\frac{\tilde{G}}{N} = \frac{A}{N} - \sum_{\substack{k=1\\k\neq l,j}}^{n} x_k\mu_k^* + \frac{b}{\rho}\frac{M}{N_A} - k_B T\boldsymbol{\alpha}:\tilde{\mathbf{c}} \tag{16}$$

where x_k is the mole fraction of chains of length k in the system.

Table 1. Details of the Molecular Model Used for Polyethylene

type of interaction	potential function and parameters
nonbonded interactions	$V_{LJ}(r_{ij}) = 4\epsilon[(\sigma_{ij}/r_{ij})^{12} - (\sigma_{ij}/r_{ij})^6]$ $\epsilon_{CH_3}/k_B = \epsilon_{CH_2}/k_B = 49.3$ K $\sigma_{CH_3} = \sigma_{CH_2} = 3.94$ Å
bond bending	$V_{bending}(\theta)/k_B = 1/2k_\theta(\theta - \theta_{eq})^2$ $k_\theta = 57\ 950$ K rad^{-2} $\theta_{eq} = 112°$
dihedral angles	$V_{tors}(\phi)/k_B = \sum_{k=0}^{5} c_k \cos^k(\phi)$ $c_0 = 1116$ K, $c_1 = 1462$ K, $c_2 = -1578$ K, $c_3 = -368$ K, $c_4 = 3156$ K, $c_5 = -3788$ K

4. Molecular Model and Simulation Strategy

Simulations of linear polyethylene were performed using a united-atom description for the methylenes and methyls. The details of the atomistic model and the exact form of the potential functions used in the simulation are given in Table 1. A finite-range modification of the Lennard-Jones potential was employed in the

simulations: the potential and its first and second derivatives were defined to be zero for $r > 2.3\sigma$, and a quintic spline was used between $r = 1.45\sigma$ and $r = 2.3\sigma$, ensuring that discontinuities occur only in the third- and higher-order derivatives of the potential.[5] Attractive tail contributions were dealt with through direct integration.[41] Lennard-Jones parameters were the same for methylenes and methyls and were set equal to the values used by Dodd and Theodorou[41] and by Pant and Theodorou.[23] Carbon−carbon bond lengths were held constant at $l = 1.54$ Å, bond angles were assumed flexible, subject to the Van der Ploeg and Berendsen bending potential,[42,43] and the Ryckaert and Bellemans[44] torsional potential was used (see Table 1).

As in ref 23, two systems of linear chains of different average molecular weights and similar molecular weight distributions have been considered. The short-chain system had number average molecular length C_{24} and polydispersity index 157/144 ≃ 1.090, corresponding to a uniform (flat) distribution of chain lengths between C_{12} and C_{36}; it will be referred to simply as "C_{24}" in the following. The long-chain system had number average molecular length C_{78} and polydispersity index 10033/9243 ≃ 1.085, corresponding to a uniform distribution of chain lengths between C_{39} and C_{117}; it will be referred to as "C_{78}" in the following. Note that, in both systems, the chain length distribution is uniform between $X/2$ and $3X/2$, with $X = n/N$ being the number-average chain length; for very long X, the polydispersity index of such a distribution assumes the limiting value 13/12 ≃ 1.083, which is very close to the values realized here and comparable to polydispersity indices achieved for real polymers with anionic polymerization. To impose these flat chain length distributions in the simulations, the relative chemical potentials μ_k^* were set equal to 0 for $X/2 \le k \le 3X/2$, and equal to $-\infty$ for $k < X/2$ or $k > 3X/2$, for $k \ne l$, $k \ne j$, with $X/2 \le l < j \le 3X/2$, as explained in ref 23.

Simulations were conducted for each of the above two systems at $b = 1$ atm and $T = 450$ K in the $NnbT\boldsymbol{\mu}^*\boldsymbol{\alpha}$ ensemble discussed in section 3. They all started from the undeformed state ($\boldsymbol{\alpha} = \mathbf{0}$), where equilibrated structures were obtained by the end-bridging Monte Carlo algorithm, and progressed on to larger values of $\boldsymbol{\alpha}$. All results reported here have been accumulated for the case of a uniaxial extensional field

$$\boldsymbol{\alpha} = \begin{pmatrix} \alpha_{xx} & 0 & 0 \\ 0 & 0 & 0 \\ 0 & 0 & 0 \end{pmatrix} \tag{17}$$

only the xx component of which is nonzero. According to eq 8, such a choice for the field $\boldsymbol{\alpha}$ implies that the two lateral normal stresses τ_{yy} and τ_{zz} are kept constant, equal to $-b$, and only the normal stress τ_{xx} along the direction of extension is large and positive. This means that the physical situation simulated when $\boldsymbol{\alpha}$ is given by eq 17 is that of a uniform uniaxial extensional flow along the x-direction, such as the situation encountered locally in a continuous fiber spinning problem. Indeed, for this type of flow, the momentum balances in the y and z directions require that the stresses τ_{yy} and τ_{zz} remain constant at $-b$ (equal to minus the atmospheric pressure exerted on the lateral surface of the drawn polymer) and only the τ_{xx} component be strongly positive. (In the actual problem, local τ_{xx} values along the fiber are related in such a way that the product $\tau_{xx}A_f$, where A_f is the local cross section of the fiber, remains constant.)

From each simulation we obtained the conformation tensor as an ensemble average of the individual molecular conformation tensors:

$$\tilde{\mathbf{c}} = \frac{1}{N}\left\langle \sum_{i=1}^{N} \tilde{\mathbf{c}}_i \right\rangle \tag{18}$$

Other monitored quantities included the average density ρ, the molecular weight distribution, the melt structure (intramolecular mer−mer pair density functions, intermolecular mer−mer pair distribution functions,[23,41] pair distribution functions for chain centers of mass in various directions), the distribution of torsion angles, and averages of the various components of the potential energy. From the $\tilde{\mathbf{c}}$ versus $\boldsymbol{\alpha}$ relationship obtained through the simulations, the thermodynamic potential $\tilde{G}$ of eq 9 relative to the equilibrium field-free state (denoted by the subscript 0) can be obtained by thermodynamic integration. The expression for $\mathrm{d}\tilde{G}$ derived from eq 10 leads to

$$\frac{\tilde{G}}{N} - \frac{\tilde{G}_0}{N} \equiv \frac{\tilde{G}}{N}(b,T,\boldsymbol{\alpha}) - \frac{\tilde{G}_0}{N}(b,T,\mathbf{0}) = -k_B T\left[\sum_{\gamma}\sum_{\delta}\int_0^{\alpha_{\gamma\delta}} \tilde{c}_{\gamma\delta}\, \mathrm{d}\alpha_{\gamma\delta}\right]_{T,b,\alpha_{[\gamma\delta]}} \tag{19}$$

The Helmholtz energy can then be obtained from eq 9 as

$$\frac{A}{N} - \frac{A_0}{N} \equiv \frac{A}{N}(T,\rho,\tilde{\mathbf{c}}) - \frac{A_0}{N}(T,\rho,\mathbf{I}) = \frac{\tilde{G}}{N} - \frac{\tilde{G}_0}{N} - b\frac{M}{N_A}\left(\frac{1}{\rho} - \frac{1}{\rho_0}\right) + k_B T\boldsymbol{\alpha}:\tilde{\mathbf{c}} \tag{20}$$

with $\rho = \rho(T,b,\boldsymbol{\alpha})$, $\rho_0 = \rho_0(T,b,\mathbf{0})$, and $\tilde{\mathbf{c}} = \tilde{\mathbf{c}}(T,b,\boldsymbol{\alpha})$.

Equation 20 remains valid for the thermodynamic potential $\tilde{G}$ defined by eq 16 in the case of the polydisperse polymers examined here; for all chain species, the imposed relative chemical potentials and resulting equilibrium mole fractions are the same in the equilibrium undeformed and all deformed states considered and therefore do not contribute to the differences $\tilde{G}/N - \tilde{G}_0/N$ and $A/N - A_0/N$.

For the C_{24} system, simulations were conducted at seven distinct nonzero values of α_{xx}: 0.0, 0.2, 0.3, 0.4, 0.5, 0.6, and 0.75. The simulation box consisted of 32 chains and $32 \times 24 = 768$ mers or interaction sites. For the C_{78} system, simulations were conducted at $\alpha_{xx} = 0.0$, 0.1, 0.2, 0.3, and 0.35. To give the reader a feeling for the strain rates involved, we mention that, for a C_{78} melt with longest (Rouse) relaxation time of about 2.5 ns, an α_{xx} of 0.1 corresponds to an elongational rate of 4×10^7 s^{-1}. This is 2−3 orders of magnitude slower than what can be simulated with NEMD. For a polymer melt of higher molecular weight and correspondingly higher relaxation time, the same α_{xx} would correspond to a lower strain rate. The thermodynamic/MC simulation approach introduced herein offers the potential of probing such small strain rates without the large noise problems plaguing MD approaches. Except for the last two values of α_{xx} (=0.3 and 0.35), the simulation box for C_{78} consisted of 10 chains and $10 \times 78 = 780$ interaction sites. The last two runs for $\alpha_{xx} = 0.3$ and 0.35, however, were conducted in a "superbox" with size

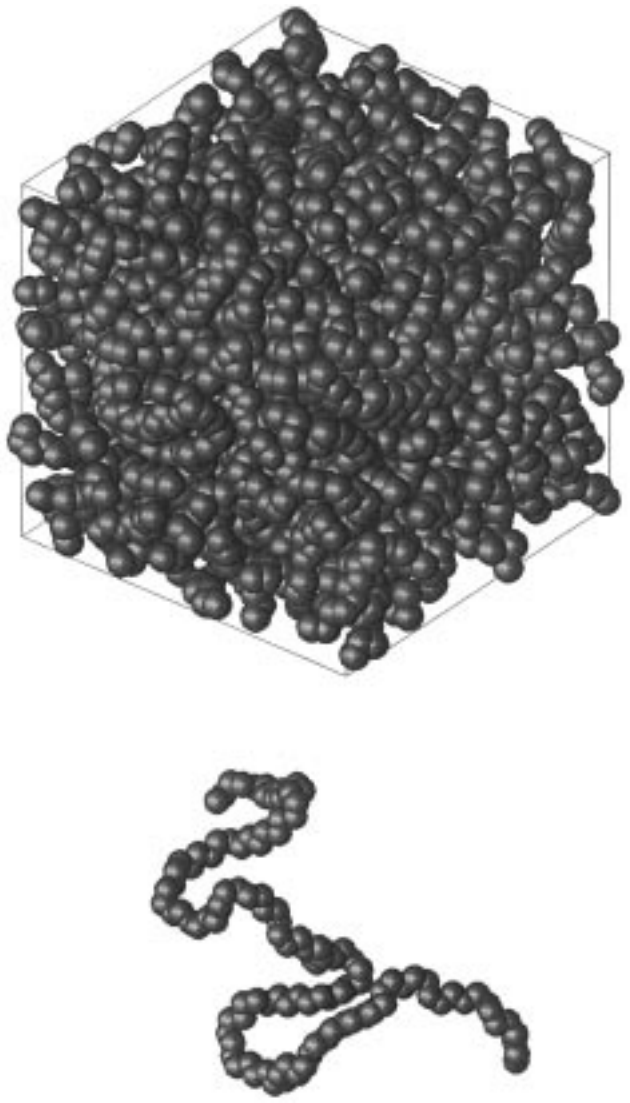

Figure 1. Periodic box (top) with 40 chains used to simulate the C_{78} chain system at high fields. There are a total of 3120 mers. Also shown (bottom) is the parent conformation of a single chain with 78 mers.

4 times larger than the previous one, containing 40 chains and a total of $40 \times 78 = 3120$ interaction sites (linear dimension ≈45 Å in each direction) (see Figure 1). This increase in size of the simulation box was found to be necessary in order to avoid system-size effects that were seen to introduce artifacts in the simulations of C_{78} in the small box for α_{xx} values larger than 0.2. Although model system size was found not to affect the equilibrium thermodynamic and structural properties of the field-free melt, a small simulation box in the presence of a strong orienting field may develop artificially highly extended conformations, induced by favorable interactions among extended images of the same chain. Thorough investigations at various box sizes were conducted to detect these artifacts and avoid them in the production runs. In the "superbox" runs, distance screening for the construction of traditional Verlet neighbor lists[1,45] to keep track of nonbonded interactions becomes excessively demanding computationally. To deal with this problem, the superbox was divided into 4^3 smaller boxes and neighbor lists were set up through a combination of Verlet and linked cell schemes.[41]

Equilibration of the system at each value of α_{xx} considered was achieved by employing the end-bridging algorithm of Pant and Theodorou.[23] The following mix of attempted moves was used: reptations, 6%; rotations, 6%; flips, 6%; concerted rotations, 32%; end-bridging, 49.5%; volume fluctuations, 0.5%.

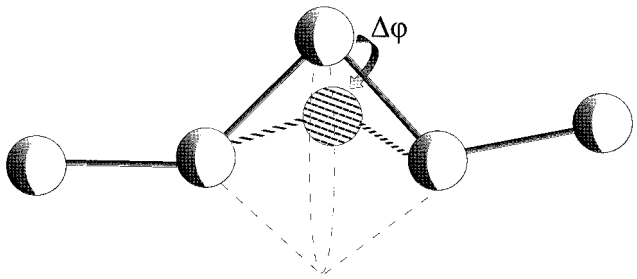

Figure 2. Schematic representation of a flip move. Original and final positions of the moved mer are shown in solid and broken lines, respectively.

A "flip" is a new, relatively simple move for atomistic chain models with flexible bond angles, in which a nonterminal mer is picked at random and rotated by an angle chosen from a uniform distribution in $(-\Delta\phi_{max}, \Delta\phi_{max})$ with $\Delta\phi_{max} = 10°$ around the axis formed by the two mers flanking it on either side (see Figure 2). In this way, four dihedral and two bond angles are changed. The move is very effective for introducing local fluctuations in atomistic models with flexible bond angles.

The concerted rotation (CONROT) move was implemented with two driver angles in Cartesian coordinates, as in ref 46. Bond angles were kept unchanged within the chain section rearranged by a CONROT move.

The ability of the connectivity-altering end-bridging MC algorithm to relax long polymer chain systems was first demonstrated by Pant and Theodorou.[23] In the present work, additional studies were performed to quantify the efficiency of the algorithm. It has been seen that, when end-bridging is employed in an MC run, the rate of decay with CPU time of the autocorrelation function for the chain end-to-end vectors in a C_{78} system is actually faster than in a C_{24} system. (Compare Figures 4a and 5a below.) Despite its very low acceptance rate (≈0.08% for both chain systems at $\boldsymbol{\alpha = 0}$), the end-bridging move is orders of magnitude more effective than any other atomistic simulation scheme we are aware of in vigorously sampling the long-range conformational properties of long-chain systems. In the present studies of oriented melts, the success rate of the move slows down somewhat as the strength of the field increases (for example, for the C_{24} system, the success rate drops from ≈0.077% at $\alpha_{xx} = 0$ to ≈0.068% at $\alpha_{xx} = 0.5$, and to ≈0.053% at $\alpha_{xx} = 0.75$, whereas for the C_{78} system, the success rate drops from ≈0.084% at $\alpha_{xx} = 0$ to ≈0.079% at $\alpha_{xx} = 0.3$); it ensures, however, true equilibration at all field values.

Comparisons between the melt response to the orienting field and the corresponding response of *continuous unperturbed chains* play an important role in the subsequent discussion. Following previous work,[23,41] we define continuous unperturbed chains (CUCs) as isolated chains governed by exactly the same potentials as our melt chains but devoid of nonlocal interactions along their contours. More specifically, the bond angle bending and torsional potentials of a CUC are identical to those listed in Table 1. The Lennard-Jones potential is also identical but active only between mers separated by 4 skeletal bonds along the contour (pentane effect), consistent with the definition of local interactions used

by Flory in his development of rotational isomeric state (RIS) models.[47] For given values of N, n, b, T, $\boldsymbol{\mu}^*$, and $\boldsymbol{\alpha}$, CUCs were sampled using configurational bias[48] and generalized reptation moves;[23] in the latter, a terminal segment is excised from one chain and appended to one of the ends of another chain. The acceptance criteria were the same as those used for the melt (compare probability density of eq 14), with the exception of bV and intermolecular energy terms.[23] MC simulations of CUCs were, of course, much less demanding computationally than those of melt systems.

The molecular weight distribution of CUCs sampled as described above turns out to be independent of $\boldsymbol{\alpha}$ and identical to that of the melt simulated under the same N, n, T, and $\boldsymbol{\mu}^*$ values.

For $\boldsymbol{\alpha} = \mathbf{0}$, the structural and conformational characteristics of chains in the well-equilibrated melt, based on our polyethylene model, are practically indistinguishable from those of CUCs.[23] This has been established with several other polyethylene models,[10,23,41,49] but is not a general conclusion for all polymers.[50] In the elasticity simulations presented in this work, the dependence of the mean-squared magnitude of the end-to-end vector of the chains in the unperturbed state, $\langle R^2\rangle_0$, on the chain length (number of mers) X is of particular importance, because it enters into the definition of the conformation tensor, eq 2. For the molecular model used in this work, detailed results for the function $\langle R^2\rangle_0 = \langle R^2\rangle_0(X)$ over a wide range of chain lengths (C_{12} to C_{117}) both with bulk melt chains and CUCs have shown that, to an excellent approximation, the characteristic ratio can be faithfully reproduced by the following algebraic equation:

$$\mathbf{C}_X \equiv \frac{\langle R^2\rangle_0}{(X-1)l^2} = \alpha_0 + \frac{\alpha_1}{X-1} + \frac{\alpha_2}{(X-1)^2} + \frac{\alpha_3}{(X-1)^3} \tag{21}$$

where $\alpha_0 = 9.13127$, $\alpha_1 = -75.18655$, $\alpha_2 = 315.74216$, and $\alpha_3 = -500.35188$. From eq 21 it is seen that $C_X = 6.42$ for the C_{24} chains and $C_X = 8.21$ for the C_{78} chains; it is also seen that the characteristic ratio at infinite chain length is $C_\infty = 9.13$. This value is significantly larger than the value 6.7 reported for real polyethylene,[47,51] because the torsional potential employed in our model enhances *trans* conformational states.[49] It should be noted, however, that recent neutron diffraction measurements on molten polyethylene[52,53] have yielded a value of $C_\infty = 7.8 \pm 0.4$ at 413 K, from which it can be inferred that the actual C_∞ at 450 K is higher than the traditionally reported value of 6.7. The recent simulation work of Yoon and collaborators,[54,55] using a different parameterization than the present work, has yielded results consistent with these higher measured values of C_∞.

5. Response of Simple Single-Chain Models

Under the assumption of noninteracting chains (eq 1 above), analytical results for the dependence of the conformation tensor $\tilde{\mathbf{c}}$ on the field $\boldsymbol{\alpha}$ in a monodisperse chain system can be obtained if we know the probability density function for the end-to-end vector $\mathbf{R}$ in the absence of the field $\boldsymbol{\alpha}$. According to eq 11, if $p_0(\mathbf{R})$ is the probability density function in the field-free state, the normalized probability density $p(\mathbf{R})$ in the presence of the field $\boldsymbol{\alpha}$ is

$$p(\mathbf{R}) = \frac{p_0(\mathbf{R}) \exp\left(\frac{3}{\langle R^2\rangle_0}\boldsymbol{\alpha}:\mathbf{RR}\right)}{\int p_0(\mathbf{R}) \exp\left(\frac{3}{\langle R^2\rangle_0}\boldsymbol{\alpha}:\mathbf{RR}\right) \mathrm{d}^3 R} \tag{22}$$

The conformation tensor components can then be found by taking the moments of the distribution function, $p(\mathbf{R})$, as follows:

$$\tilde{c}_{\alpha\beta} = \frac{3}{\langle R^2\rangle_0} \frac{\int_0^\infty R_\alpha R_\beta p_0(\mathbf{R}) \exp\left(\frac{3}{\langle R^2\rangle_0}\boldsymbol{\alpha}:\mathbf{RR}\right) \mathrm{d}^3 R}{\int_0^\infty p_0(\mathbf{R}) \exp\left(\frac{3}{\langle R^2\rangle_0}\boldsymbol{\alpha}:\mathbf{RR}\right) \mathrm{d}^3 R} \tag{23}$$

For the case of the uniaxial extensional field considered in the present work, eq 23 simplifies to

$$\tilde{c}_{\alpha\beta} = \frac{3}{\langle R^2\rangle_0} \frac{\int_0^\infty R_\alpha R_\beta p_0(\mathbf{R}) \exp\left(\frac{3}{\langle R^2\rangle_0}\alpha_{xx}R_x^2\right) \mathrm{d}^3 R}{\int_0^\infty p_0(\mathbf{R}) \exp\left(\frac{3}{\langle R^2\rangle_0}\alpha_{xx}R_x^2\right) \mathrm{d}^3 R} \tag{24}$$

Gaussian Model. For a 3-dimensional Gaussian chain, $p_0(\mathbf{R})$ is given by[25,37]

$$p_0(\mathbf{R}) = \left(\frac{3}{2\pi\langle R^2\rangle_0}\right)^{3/2} \exp\left(-\frac{3}{2}\frac{R^2}{\langle R^2\rangle_0}\right) \tag{25}$$

with R being the length of the vector $\mathbf{R}$. The end-to-end vector of a Gaussian chain behaves as an "elastic" or "Hookean dumbbell". In mapping our atomistic polyethylene chains onto the Gauss model, we choose $\langle R^2\rangle_0$ to be the same for the Gaussian chains as for the atomistic chains in their field-free unperturbed (or melt) state.

Substituting eq 25 into eq 24 and performing the integrations gives

$$\tilde{c}_{xx} = \frac{1}{1-2\alpha_{xx}}$$

$$\tilde{c}_{yy} = 1$$

$$\tilde{c}_{zz} = 1$$

$$\tilde{c}_{\gamma\delta} = 0 \qquad \text{for} \qquad \gamma \neq \delta \tag{26}$$

The Gaussian chain model predicts zero off-diagonal components of the conformation tensor, no effect of the field α_{xx} on $\tilde{c}_{yy}$ and $\tilde{c}_{zz}$, and a $\tilde{c}_{xx}$ component that increases rapidly with increasing α_{xx}. The insensitivity of $\tilde{c}_{yy}$ and $\tilde{c}_{zz}$ to α_{xx} stems from the independence of the distributions of the three Cartesian components of $\mathbf{R}$. The model predicts that $\tilde{c}_{xx}$ will diverge for $\alpha_{xx} = 0.5$. This is a consequence of the infinite extensibility of the Gaussian model; it is intimately related to the divergence of the elongational viscosity for the Maxwell model at a value of the dimensionless elongation rate (tensile strain rate times chain relaxation time) equal to 0.5, discussed by Bird *et al.* (ref 20, Vol 2, p 75, see also discussion of stresses in section 6).

Using eqs 19 and 20 in conjunction with eq 26, we obtain the Helmholtz energy function for the purely elongational case considered here:

$$\frac{A}{N}(T,\rho,\tilde{\mathbf{c}}) - \frac{A_0}{N}(T,\rho,\mathbf{I}) = \frac{1}{2}k_BT(\tilde{c}_{xx} - 1) - \frac{1}{2}k_BT \ln \tilde{c}_{xx} = \frac{1}{2}k_BT(\tilde{c}_{xx} + 2) - \frac{1}{2}k_BT \ln \tilde{c}_{xx} - \frac{3}{2}k_BT \quad (27)$$

which is consistent with the more general expression given by Beris and Edwards[33] for Gaussian chains:

$$\frac{A}{N}(T,\rho,\tilde{\mathbf{c}}) = \frac{A_{liq}}{N}(T,\rho) + \frac{1}{2}k_BT \,\mathrm{Tr}(\tilde{\mathbf{c}}) - \frac{1}{2}k_BT \ln[\det(\tilde{\mathbf{c}})] \quad (28)$$

Freely-Jointed Chain Model. For a freely-jointed chain, $p_0(\mathbf{R})$ depends on the number of links N_K, and in its most general form is given by the Rayleigh equation:[37,47]

$$p_0(\mathbf{R}) = \frac{1}{2\pi^2 R}\int_0^\infty \sin(\rho R)\left(\frac{\sin(\rho b_K)}{\rho b_K}\right)^{N_K} \rho \, d\rho \quad (29)$$

with b_K being the length of the link. For small N_K's ($N_K = 2-6$), the integral can be evaluated analytically through the use of trigonometric identities.[37,47]

In mapping our atomistic polyethlylene chains onto the freely-jointed chain model, we choose b_K to be equal to the Kuhn segment length of infinitely long atomistic polyethylene chains. N_K then stands for the number of Kuhn segments corresponding to the chain length of our polyethylene melts. More specifically,

$$b_K = \frac{lC_\infty}{\sin\left(\frac{\theta_{eq}}{2}\right)} = \frac{\langle R^2\rangle_0}{L} \quad (30)$$

and

$$N_K = \frac{\langle R^2\rangle_0}{{b_K}^2} \quad (31)$$

with θ_{eq} being the equilibrium bond angle in the atomistic model and L the contour length of the chain at full extension. Values for b_K and N_K are given in the next section, where the melt response is compared against that of the simple theoretical models.

Substituting eq 29 for $p_0(\mathbf{R})$ into eq 24 and carrying out the integrations in polar coordinates yields

$$\tilde{c}_{xx} = \frac{\int_0^1 f_{N_K}(x)\left(\int_0^{\sqrt{3N_Kx^2}} \omega^2 \exp(\alpha_{xx}\omega^2)\, d\omega\right) dx}{\int_0^1 f_{N_K}(x)\left(\int_0^{\sqrt{3N_Kx^2}} \exp(\alpha_{xx}\omega^2)\, d\omega\right) dx}$$

$$\tilde{c}_{yy} = \frac{1}{2}(3\langle\tilde{R}^2\rangle - \tilde{c}_{xx})$$

$$\tilde{c}_{zz} = \frac{1}{2}(3\langle\tilde{R}^2\rangle - \tilde{c}_{xx})$$

$$\tilde{c}_{\gamma\delta} = 0 \quad \text{for} \quad \gamma \neq \delta \quad (32)$$

where

$$\langle\tilde{R}^2\rangle \equiv \frac{\langle R^2\rangle}{\langle R^2\rangle_0} = N_K \frac{\int_0^1 x^2 f_{N_K}(x)\left(\int_0^{\sqrt{3N_Kx^2}} \exp(\alpha_{xx}\omega^2)\, d\omega\right) dx}{\int_0^1 f_{N_K}(x)\left(\int_0^{\sqrt{3N_Kx^2}} \exp(\alpha_{xx}\omega^2)\, d\omega\right) dx} \quad (33)$$

In eqs 32 and 33, $\langle\tilde{R}^2\rangle$ is the mean-squared chain end-to-end distance, reduced by its unperturbed value, as a function of the imposed field α_{xx}, and $f_{N_K}(x)$ with $x = R/(N_K b_K)$ is a scaled form of the equilibrium distribution function $p_0(\mathbf{R})$, defined so that the outer limits of the integration in eqs 32 and 33 are 0 and 1. $f_{N_K}(x)$ depends on the number of Kuhn segments making up the chain; for $N_K = 1-6$, it can be derived by the expression reported by Flory,[47] and is given in Appendix C in the form used in eqs 32 and 33.

As can be seen from the form of eq 32, a purely extensional field α_{xx} will not induce nonzero off-diagonal elements of the conformation tensor in the freely-jointed chain model, exactly as happens with the Gaussian model. In contrast to the Gaussian model, however, α_{xx} will affect not only $\tilde{c}_{xx}$ but also the other diagonal elements $\tilde{c}_{yy}$ and $\tilde{c}_{zz}$. This is due to the finite extensibility of freely-jointed chains.

FENE Model. The finite extensibility nonlinear elastic dumbbell (FENE) model[20] describes the polymer chain as an elastic dumbbell with a maximum extension length L and a spring constant H. According to this model, the equilibrium distribution function for the end-to-end vector is given by

$$p_0(\mathbf{R}) = \begin{cases} \text{const}\,[1 - (R/L)^2]^{HL^2/(2k_BT)} & \text{if } r < L \\ 0 & \text{if } r \geq L \end{cases} \quad (34)$$

The Gauss model is recovered from the FENE model in the limit

$$B \equiv \frac{HL^2}{k_BT} \to \infty \quad (35)$$

In addition, the mean-squared end-to-end distance is given by [ref 20, Vol 2, p 79]

$$\langle R^2\rangle_0 = \frac{3L^2}{B+5} = \frac{3k_BT}{H}\frac{B}{B+5} \quad (36)$$

In mapping our atomistic polyethylene chains onto the FENE model, we identify L with the contour length of the atomistically represented chain:

$$L = (X-1)l \sin\frac{\theta_{eq}}{2} \quad (37)$$

and we demand that the value of $\langle R^2\rangle_0$ given by eq 36 be the same as the value of $\langle R^2\rangle_0$ calculated from the simulations of the unoriented chains (compare eq 21). This leads to assigning to B the value

$$B = \frac{3L^2}{\langle R^2\rangle_0} - 5 \quad (38)$$

or setting the Hookean spring constant H equal to

$$H = \frac{3k_BT}{\langle R^2\rangle_0} - \frac{5k_BT}{L^2} \quad (39)$$

Clearly, as $L \rightarrow \infty$, i.e., for infinitely extensible chains, $H \rightarrow 3k_BT/\langle R^2\rangle_0$, and we recover the Gaussian limit.

Substituting eq 34 for $p_0(\mathbf{R})$ into eq 23 for $\tilde{\mathbf{c}}$ and carrying out the integrations in polar coordinates gives

$$\tilde{c}_{xx} = \frac{\int_0^1 x(1-x^2)^{B/2}\left(\int_0^{\sqrt{(B+5)x^2}} \omega^2 \exp(\alpha_{xx}\omega^2)\, d\omega\right) dx}{\int_0^1 x(1-x^2)^{B/2}\left(\int_0^{\sqrt{(B+5)x^2}} \exp(\alpha_{xx}\omega^2)\, d\omega\right) dx}$$

$$\tilde{c}_{yy} = \frac{1}{2}(3\langle\tilde{R}^2\rangle - \tilde{c}_{xx})$$

$$\tilde{c}_{zz} = \frac{1}{2}(3\langle\tilde{R}^2\rangle - \tilde{c}_{xx})$$

$$\tilde{c}_{\gamma\delta} = 0 \qquad \text{for} \qquad \gamma \neq \delta \tag{40}$$

where

$$\langle\tilde{R}^2\rangle \equiv \frac{\langle R^2\rangle}{\langle R^2\rangle_0} = \frac{B+5}{3}\frac{\int_0^1 x^3(1-x^2)^{B/2}\left(\int_0^{\sqrt{(B+5)x^2}} \exp(\alpha_{xx}\omega^2)\, d\omega\right) dx}{\int_0^1 x(1-x^2)^{B/2}\left(\int_0^{\sqrt{(B+5)x^2}} \exp(\alpha_{xx}\omega^2)\, d\omega\right) dx} \tag{41}$$

As the freely-jointed chain model, the FENE model also predicts zero off-diagonal components of the conformation tensor, and an effect of the field α_{xx} on all diagonal elements $\tilde{c}_{xx}$, $\tilde{c}_{yy}$, and $\tilde{c}_{zz}$.

6. Simulation Results and Discussion

We present here structural and thermodynamic results obtained for the C_{24} and C_{78} systems under the conditions stated in section 4, for various values of the extensional field α_{xx}.

Effect of the Field on the Density and Molecular Weight Distribution. A first question one may ask is whether the orienting field has any effect on the density and molecular weight distribution of the C_{24} and C_{78} systems, simulated under given values of N, n, b, T, and $\boldsymbol{\mu}^*$. Figure 3a shows the effect of α_{xx} on the specific volume $1/\rho$. Some slight decrease of the specific volume is seen to take place for the C_{24} system at the higher values of α_{xx} (>0.4) studied. Nevertheless, for long chains and low fields, which are most relevant to actual rheological applications, we can conclude that the field does not essentially alter the density of the system. Similarly, Figure 3b shows that the field α_{xx} has no effect on the molecular weight distribution of the simulated melt: for all α_{xx}'s examined, the distribution of chain lengths remained uniform, exactly as when no field was applied. The same observation was made also for the CUC systems we studied; there, the lower computational requirements of the simulation permitted a much lower statistical uncertainty in the determination of the chain length distribution than in the melt.

Equilibration of Long-Range Conformational Characteristics. Figures 4 and 5 show results for the equilibration of the C_{24} and C_{78} systems, respectively, for a zero and a non-zero value of the field α_{xx}. For the simulations with a non-zero value of α_{xx}, a well-equilibrated unstrained melt configuration was used as the initial configuration in both cases. As mentioned in section 4, the two simulated systems contain roughly the same total number of monomer units. The top parts in the figures display the decay of the autocorrelation function $\langle\mathbf{u}(t)\cdot\mathbf{u}(0)\rangle$ for a unit vector $\mathbf{u}$ directed along the chain end-to-end vector, and the bottom ones track the evolution of the diagonal components of the conformation tensor with CPU time on an IBM RS/6000 3CT workstation. The dashed curve on the top part of each figure corresponds to the equilibrium unstrained melt, whereas the solid curve corresponds to the strained melt. For both the unstrained and the strained melts, the function $\langle\mathbf{u}(t)\cdot\mathbf{u}(0)\rangle$ decays to a zero value within the error of the simulation. In the presence of the field α_{xx}, this decay is somewhat slower than in the equilibrium unstrained melt by a factor that depends on the value of α_{xx}. For example, for the C_{24} system and $\alpha_{xx} = 0.2$, this factor is $\approx$22%, while for the C_{78} system and $\alpha_{xx} = 0.2$, this factor is $\approx$10%. As mentioned in section 4, this happens because chain orientation reduces somewhat the success rate of end-bridging moves. Comparison of the dashed curves in Figures 4a and 5a shows that the end-to-end vector autocorrelation function decays *faster* in the long-chain system; this remarkable feature of the end-bridging algorithm will be explained and quantified in a forthcoming publication.

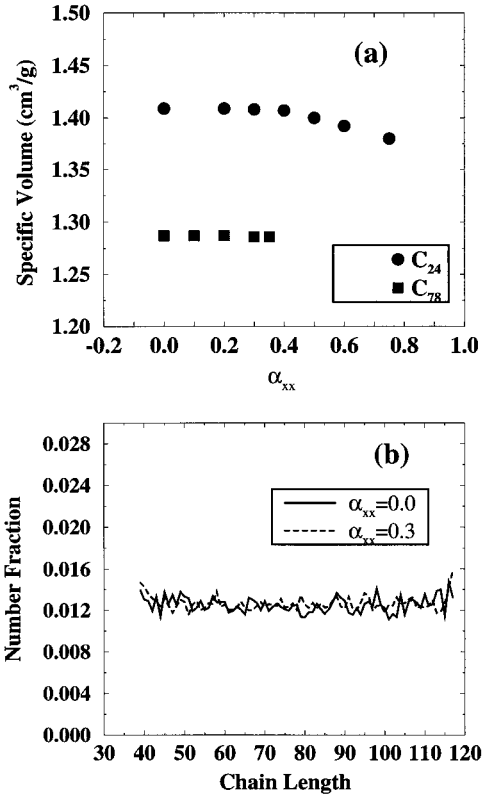

Figure 3. Effect of the orienting field α_{xx} on (a) the density of the C_{24} and C_{78} chain systems and (b) the chain length distribution of the C_{78} polymer melt (T = 450 K and b = 1 atm).

The diagonal components of $\tilde{\mathbf{c}}$ in Figures 4b and 5b are seen to relax to well-defined values, characteristic of the strained melt; the CPU time needed for equilibrating $\tilde{\mathbf{c}}$, however, is 5−10 times longer than that needed for $\langle\mathbf{u}(t)\cdot\mathbf{u}(0)\rangle$ to decay to its limiting value of zero. Furthermore, roughly 3 times more CPU time is needed for the components of $\tilde{\mathbf{c}}$ (especially $\tilde{c}_{xx}$) to reach a well-defined plateau value in the C_{78} system than in the C_{24} system. This is probably due to the smaller number of chains present in the longer-chain system

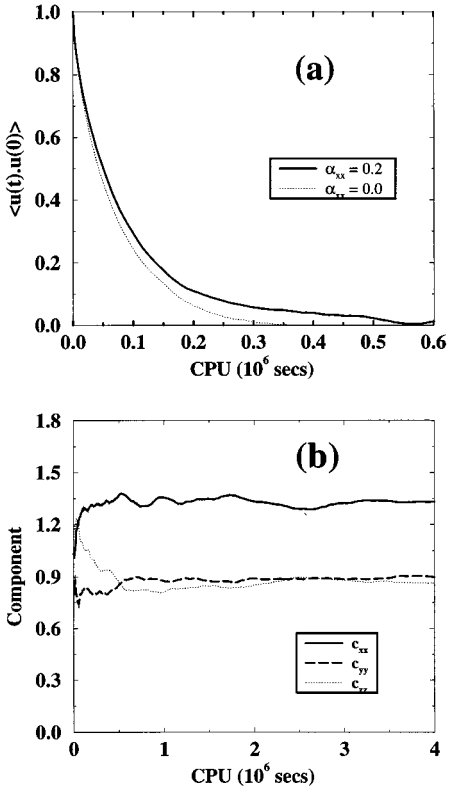

Figure 4. Evolution of (a) the chain end-to-end vector orientational autocorrelation function $\langle \mathbf{u}(t)\cdot\mathbf{u}(0)\rangle$ and (b) the diagonal (non-zero) components of the conformation tensor $\tilde{\mathbf{c}}$ with CPU time for $\alpha_{xx} = 0.2$ in the C_{24} melt system at $T = 450$ K and $b = 1$ atm. CPU times are on an IBM RS/6000 3CT workstation.

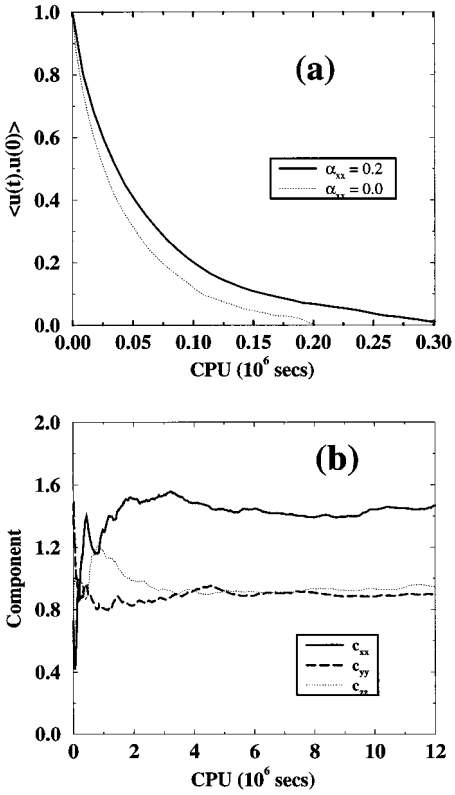

Figure 5. Evolution of (a) the chain end-to-end vector orientational autocorrelation function $\langle \mathbf{u}(t)\cdot\mathbf{u}(0)\rangle$ and (b) the diagonal components of the conformation tensor $\tilde{\mathbf{c}}$ with CPU time for $\alpha_{xx} = 0.2$ in the C_{78} melt system at $T = 450$ K and $b = 1$ atm. CPU times are on an IBM RS/6000 3CT workstation.

and to the much larger intrinsic variance of the **R** distribution in that system. Approximately 20 days on an IBM 3CT are required to get a reliable estimate of $\tilde{c}_{xx}$ for the C_{78} system. This reflects the computational difficulty of predicting the elasticity and, in general, the viscoelastic response of long-chain melts in the terminal region. The free energy calculations reported here would have been utterly impossible without the vigorous sampling of long-range conformational features afforded by the end-bridging move.

In both systems, $\tilde{c}_{xx}$ reaches an equilibrium value significantly larger than 1, while $\tilde{c}_{yy}$ and $\tilde{c}_{zz}$ converge to a common value, as required by the cylindrical symmetry of the orienting field; that common value is smaller than 1 (see below).

Chain End-to-End Distance and Conformation Tensor as Functions of the Orienting Field. Figure 6 shows the effect of α_{xx} on the mean-squared end-to-end distance of the polymer chains. The solid line displays results for the chains studied in strained melt systems ($\alpha_{xx} = 0.3$), and the thick dashed line displays results for CUCs in the absence of a field ($\alpha_{xx} = 0.0$); as already mentioned, the latter reproduce almost perfectly the conformational characteristics of chains in the equilibrium unstrained melt. Clearly, α_{xx} has a strong effect on the end-to-end distance of the chains. For the field-free CUCs, $\langle R^2\rangle = \langle R^2\rangle_0$ is given by eq 21; Figure 6 shows that, for the chain lengths X examined, it is in fact a linear function of X. For $\alpha_{xx} \neq 0$, the relationship between $\langle R^2\rangle$ and chain length in the melt is convex downward (long chains being more affected by the field), in disagreement with the simple Gaussian model, eq 26, which predicts a linear relation, and in qualitative

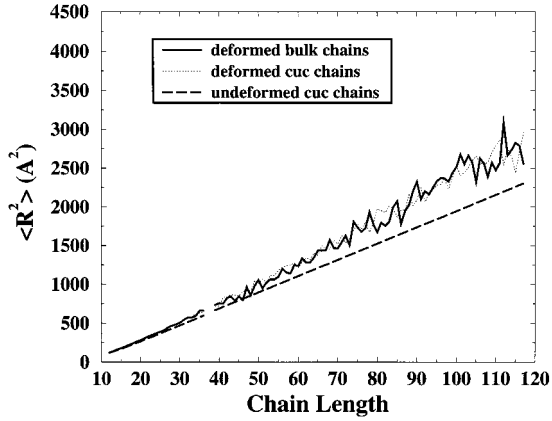

Figure 6. Chain mean-squared end-to-end distance as a function of chain length ($T = 450$ K, $b = 1$ atm). Results obtained from both the C_{24} system (chain lengths 12−36) and the C_{78} system (chain lengths 39−117) are shown on the same plot. The thick solid line tracks $\langle R^2\rangle$ for bulk melt chains at $\alpha_{xx} = 0.3$, and the thin dotted line tracks the same quantity for continuous unperturbed chains (CUCs) subjected to the same field ($\alpha_{xx} = 0.3$). The thick long-dashed line shows $\langle R^2\rangle$ for CUCs at $\alpha_{xx} = 0.0$ (equilibrium unstrained case).

agreement with the freely-jointed chain and FENE models, eqs 33 and 41, which also predict that longer chains are more affected by the field (see also Tables 2 and 3). Also shown in Figure 6 is the curve obtained for continuous unperturbed chains (CUCs) subjected to the same orienting field as the melt chains (dotted line). Clearly, the effect of the field on $\langle R^2\rangle$ is very similar for bulk melt chains and CUCs.

Parts a and b of Figure 7 show the effect of α_{xx} on the individual components of the conformation tensor $\tilde{c}_{xx}$,

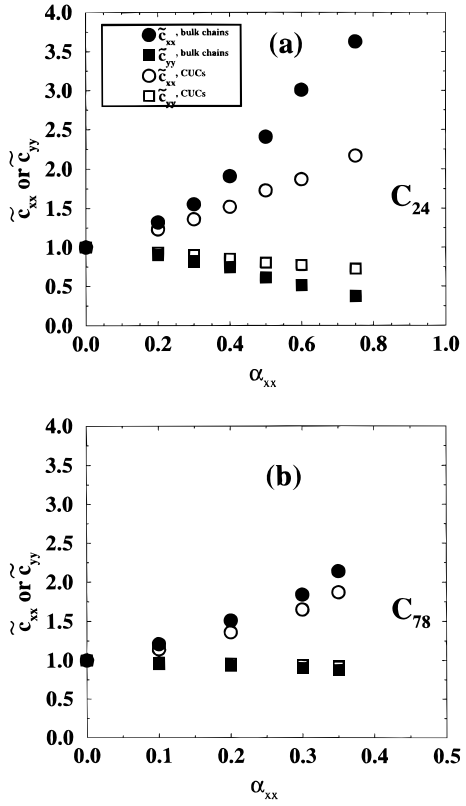

Figure 7. Diagonal components of the conformation tensor $\tilde{\mathbf{c}}$ as functions of the orienting field α_{xx}, for (a) the C_{24} system and (b) the C_{78} system. Filled symbols show the results for bulk melt chains, and open symbols for CUCs ($T = 450$ K, $b = 1$ atm). The statistical error in the bulk results is approximately equal to the size of the symbols.

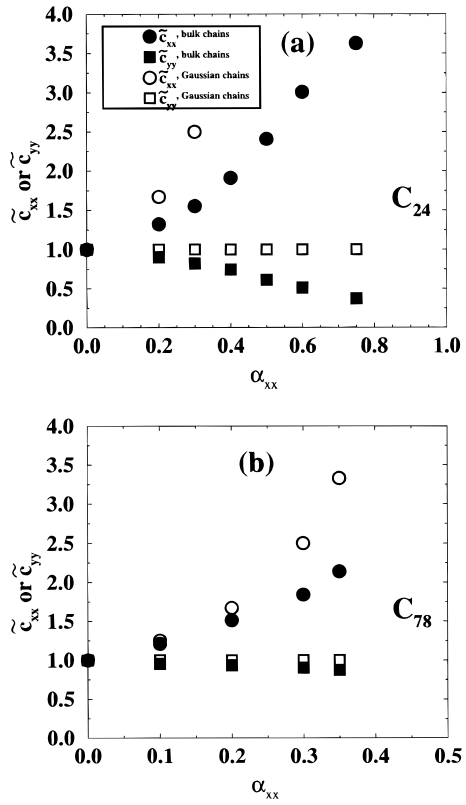

Figure 8. Diagonal components of the conformation tensor $\tilde{\mathbf{c}}$ as functions of the orienting field α_{xx}, for (a) the C_{24} system and (b) the C_{78} system. Filled symbols show the results for bulk melt chains, and open symbols the analytical predictions of the Gaussian model ($T = 450$ K, $b = 1$ atm).

Table 2. Mean-Squared End-to-End Distance ($\langle \tilde{R}^2 \rangle$) Reduced by Its Unperturbed Value for the C_{24} Chain System as a Function of the Orienting Field α_{xx} from Simulations of Bulk Melt Chains and CUCs and from the Three Theoretical Models Examined in the Present Work ($T = 450$ K and $b = 1$ atm)

α_{xx}	bulk chains	CUCs	Gaussian	freely-jointed	FENE
0.00	0.99 ± 0.02	1.00	1.00	1.00	1.00
0.20	1.04 ± 0.02	1.03	1.22	1.02	1.07
0.30	1.08 ± 0.02	1.08	1.50	1.03	1.12
0.40	1.16 ± 0.03	1.11	2.33	1.05	1.18
0.50	1.29 ± 0.04	1.16	∞	1.06	1.25
0.60	1.43 ± 0.07	1.20	∞	1.08	1.32
0.75	1.56 ± 0.10	1.25	∞	1.10	1.44

Table 3. Mean-Squared End-to-End Distance ($\langle \tilde{R}^2 \rangle$) Reduced by Its Unperturbed Value for the C_{78} Chain System as Function of the Orienting Field α_{xx} from Simulations of Bulk Melt Chains and CUCs and from the Three Theoretical Models Examined in the Present Work ($T = 450$ K and $b = 1$ atm)

α_{xx}	bulk chains	CUCs	Gaussian	freely-jointed	FENE
0.00	0.98 ± 0.04	1.00	1.00	1.00	1.00
0.10	1.04 ± 0.03	1.03	1.08	1.06	1.06
0.20	1.12 ± 0.04	1.09	1.22	1.15	1.14
0.30	1.18 ± 0.03	1.17	1.50	1.28	1.26
0.35	1.27 ± 0.05	1.24	1.77	1.36	1.33

$\tilde{c}_{yy}$, and $\tilde{c}_{zz}$ for the C_{24} and C_{78} systems, respectively. The filled symbols are results from bulk melt simulations, and the open symbols from CUCs subjected to the same orienting field. Clearly, there are significant differences between the two types of chains in the response of their conformation tensor to the orienting field: bulk melt chains tend to adopt more anisotropic shapes (higher $\tilde{c}_{xx}$, lower $\tilde{c}_{yy}$) than CUCs. For relatively low fields, this difference is modest: At $\alpha_{xx} = 0.3$, for example, $\tilde{c}_{xx}$ is by 12% higher for bulk chains than it is for CUC chains. The gap between melt response and CUC response becomes huge, however, for the high fields ($\alpha_{xx} > 0.4$) explored with the C_{24} system.

From eqs 10, 19 and 20 it is seen that $\tilde{\mathbf{c}}$ is the derivative of the thermodynamic potential $\tilde{G}/N$ with respect to the orienting field $\boldsymbol{\alpha}$, allowing the Helmholtz energy function $A/N(T,\rho,\tilde{\mathbf{c}})$ to be reconstructed as a function of the conformation tensor (see below). Therefore, all plots of $\tilde{\mathbf{c}}$ vs $\boldsymbol{\alpha}$ can be viewed as providing the desired fundamental equation for the dependence of A/N upon $\tilde{\mathbf{c}}$. It is therefore instructive to compare the $\tilde{\mathbf{c}}(\boldsymbol{\alpha})$ relation extracted from our atomistic simulations against the corresponding relations predicted on the basis of simple models of chain elasticity, such as those discussed in section 5. Figures 8−10 show this comparison against the Gaussian (Hookean dumbbell), freely-jointed chain and FENE models, respectively. Calculations with the simple models were based on eqs 26, 32, and 40, respectively.

The analytical results for the freely-jointed chain model have been obtained for a value of $b_K = 16.7$ Å, and for $N_K = 1.25$ for the C_{24} chains and $N_K = 5.34$ for the C_{78} chains (compare eqs 30 and 31). Noninteger values of N_K were dealt with by linear interpolation of the analytical results obtained for the integer values $[N_K]$ and $[N_K] + 1$ at each field value. (Here, $[N_K]$ symbolizes the integer part of N_K.) The analytical results for the FENE model have been obtained for values of $B = 2.39$ and $L = 29.36$ Å for the C_{24} chains and $B = 14.35$ and $L = 98.31$ Å for the C_{78} chains

Table 4. Conformation Tensor Components for the C_{24} Chain System as Functions of the Orienting Field α_{xx} from Simulations of Bulk Melts and CUCs and from the Three Theoretical Models Examined in the Present Work (T = 450 K and b = 1 atm)

	bulk chains		CUCs		Gaussian		freely-jointed		FENE	
α_{xx}	$\tilde{c}_{xx}$	$\tilde{c}_{yy}$	$\tilde{c}_{xx}$	$\tilde{c}_{yy}$	$\tilde{c}_{xx}$	$\tilde{c}_{yy}$	$\tilde{c}_{xx}$	$\tilde{c}_{yy}$	$\tilde{c}_{xx}$	$\tilde{c}_{yy}$
0.00	1.03 ± 0.05	0.99 ± 0.04	1.00	1.00	1.00	1.00	1.00	1.00	1.00	1.00
0.20	1.32 ± 0.05	0.90 ± 0.04	1.23	0.93	1.67	1.00	1.21	0.93	1.33	0.95
0.30	1.55 ± 0.06	0.82 ± 0.04	1.36	0.90	2.50	1.00	1.33	0.88	1.54	0.91
0.40	1.91 ± 0.06	0.74 ± 0.04	1.52	0.85	5.00	1.00	1.46	0.84	1.79	0.87
0.50	2.41 ± 0.09	0.61 ± 0.05	1.73	0.80	∞	1.00	1.60	0.79	2.08	0.83
0.60	3.01 ± 0.1	0.51 ± 0.04	1.89	0.78	∞	1.00	1.74	0.74	2.40	0.78
0.75	3.66 ± 0.13	0.37 ± 0.04	2.17	0.72	∞	1.00	1.95	0.67	2.93	0.70

Table 5. Conformation Tensor Components for the C_{78} Chain System as Functions of the Orienting Field α_{xx} from Simulations of Bulk Melts and CUCs and from the Three Theoretical Models Examined in the Present Work (T = 450 K and b = 1 atm)

	bulk chains		CUCs		Gaussian		freely-jointed		FENE	
α_{xx}	$\tilde{c}_{xx}$	$\tilde{c}_{yy}$	$\tilde{c}_{xx}$	$\tilde{c}_{yy}$	$\tilde{c}_{xx}$	$\tilde{c}_{yy}$	$\tilde{c}_{xx}$	$\tilde{c}_{yy}$	$\tilde{c}_{xx}$	$\tilde{c}_{yy}$
0.00	0.95 ± 0.06	0.97 ± 0.06	1.00	1.00	1.00	1.00	1.00	1.00	1.00	1.00
0.10	1.21 ± 0.06	0.95 ± 0.06	1.14	0.97	1.25	1.00	1.21	0.99	1.20	0.99
0.20	1.51 ± 0.11	0.93 ± 0.06	1.36	0.96	1.67	1.00	1.50	0.98	1.48	0.97
0.30	1.84 ± 0.13	0.90 ± 0.05	1.65	0.94	2.50	1.00	1.92	0.96	1.87	0.95
0.35	2.14 ± 0.15	0.87 ± 0.05	1.87	0.92	3.33	1.00	2.20	0.94	2.12	0.94

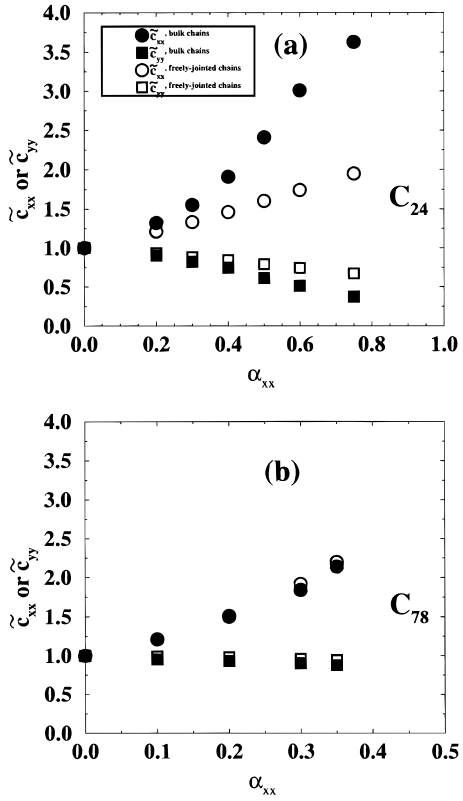

Figure 9. Diagonal components of the conformation tensor $\tilde{\mathbf{c}}$ as functions of the orienting field α_{xx}, for (a) the C_{24} system and (b) the C_{78} system. Filled symbols show the results for bulk melt chains, and open symbols the analytical predictions of the freely-jointed chain model (T = 450 K, b = 1 atm).

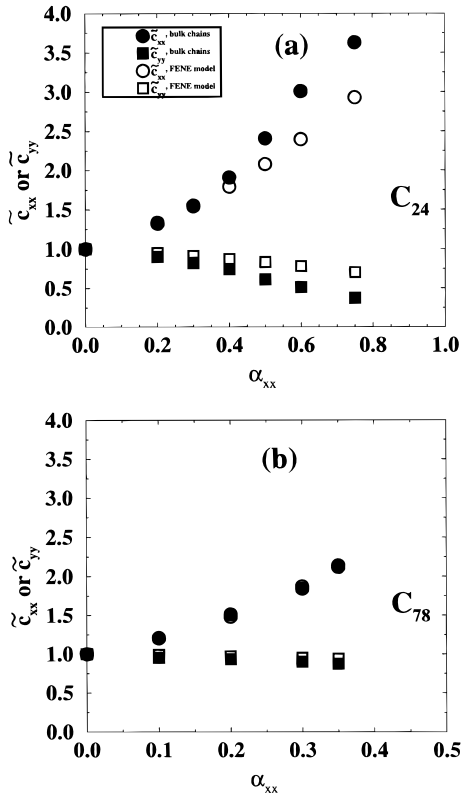

Figure 10. Diagonal components of the conformation tensor $\tilde{\mathbf{c}}$ as functions of the orienting field α_{xx}, for (a) the C_{24} system and (b) the C_{78} system. Filled symbols show the results for bulk melt chains, and open symbols the analytical predictions of the FENE model (T = 450, b = 1 atm).

(compare eqs 37 and 38). The integrals appearing in eqs 32 and 33 and eqs 40 and 41 were calculated numerically in polar coordinates, with a Gauss quadrature scheme and a relative error $<10^{-6}$. Representative results for a variety of field strengths $\boldsymbol{\alpha}$ and for all models are shown in Figures 8−10 and also summarized in Tables 4 and 5.

As seen in Figure 8, the Gaussian chain model provides but a poor representation of the orientation dependence of the Helmholtz energy in our melt system. At a given value of α_{xx}, $\tilde{c}_{xx}$ is grossly overpredicted by the Gaussian model; it actually diverges as $\alpha_{xx} \rightarrow {}^1/_2$, as discussed in section 5. On the other hand, $\tilde{c}_{xx}$ and $\tilde{c}_{yy}$ remain unaffected by α_{xx} according to the Gaussian model (compare eqs 26), while they decrease with increasing α_{xx} in the simulated melt. These deficiencies are due to the fact that the Gaussian model does not incorporate any information regarding the finite extensibility of the chains. Only in the limit of very long chains and very low orientational fields can the Gauss model provide a reasonable representation of reality. One would expect that, if more information about the

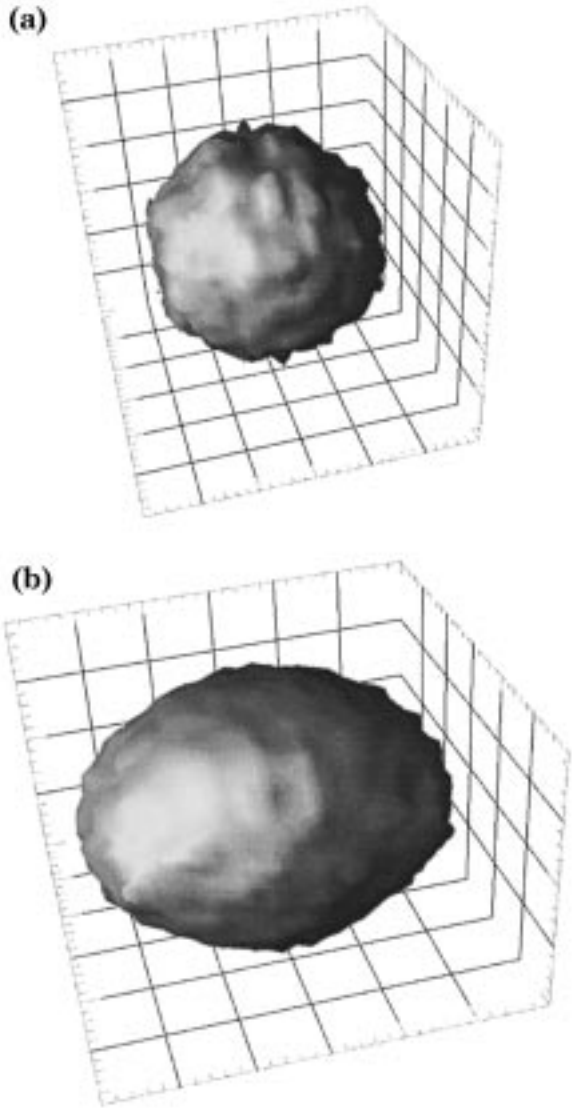

Figure 11. Surfaces of equal average segment density in the laboratory frame, for (a) undeformed ($\alpha_{xx} = 0.0$) and (b) uniaxially stretched ($\alpha_{xx} = 0.3$) C_{78} systems. The surfaces are drawn for a segment density equal to 0.35 mers/nm^3 and contain 87.5% and 83.2% of the total segments, respectively ($T = 450$ K, $b = 1$ atm). The distance between successive grid lines on the axes of the figure represents 12.45 Å of real length.

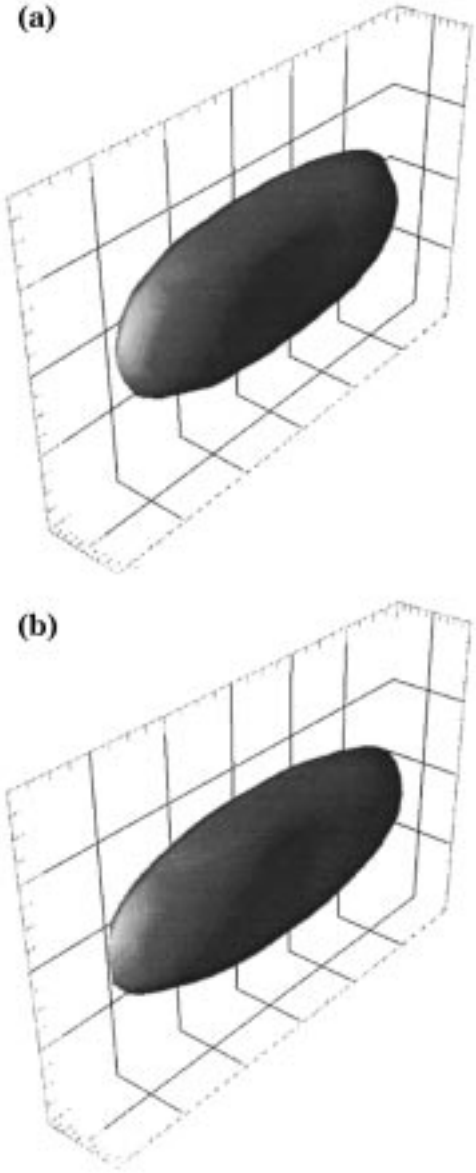

Figure 12. Surfaces of equal average segment density in the frame of the principal axes of the instantaneous radius of gyration tensor: (a) undeformed ($\alpha_{xx} = 0.0$) and (b) uniaxially stretched ($\alpha_{xx} = 0.3$) C_{78} system. The surfaces are drawn for a segment density equal to 5.0 mers/nm^3 and contain 59.2% and 56.3% of the total segments, respectively ($T = 450$ K, $b = 1$ atm). The distance between successive grid lines on the axes of the figure represents 9.96 Å of real length.

finite extensibility of chains is incorporated in the simple theoretical models, agreement between the simple models and simulation results will improve. This is indeed confirmed by the comparison with the freely-jointed chain and FENE models.

The singularity presented by the Gaussian model for $\alpha_{xx} = 0.5$ is removed in the freely-jointed chain and FENE models. In the C_{24} system, freely-jointed chains assume a less anisotropic shape than melt chains in the presence of the field. In fact, the response of freely-jointed chains for this system is remarkably similar to that of CUCs, displayed in Figure 7. In the C_{78} system, where N_K is significantly larger than 1, the freely-jointed chain response is very close to that of the melt. Results for FENE chains reproduce the response of both C_{24} and C_{78} melts for low fields ($\alpha_{xx} < 0.4$) almost quantitatively. The FENE response is less anisotropic than the melt response for $\alpha_{xx} > 0.4$ in the C_{24} system. For the C_{78} chains, the freely-jointed chain and FENE models predict the $\tilde{\mathbf{c}}(\alpha)$ relation of the melt within about 8% and 5% of the simulation results, respectively. We can infer, therefore, that the freely-jointed chain and, especially, the FENE model, with parameters chosen as discussed in section 5, can quite satisfactorily describe the elasticity of unentangled polymer melts in the region of low elongational strain rates that is most relevant to applications.

Shape of Chain Segment Cloud in the Oriented Melt. The molecular orientation induced by the extensional field can be seen more clearly by visualizing the segment cloud of melt chains for various α_{xx} values. Figure 11 displays the density distribution of segments around the chain center of mass in the laboratory frame, averaged over all chains encountered in the C_{78} melt system. Results are shown for chains in the undeformed ($\alpha_{xx} = 0.0$) and uniaxially stretched ($\alpha_{xx} = 0.3$) melt. The distributions are visualized here as three-dimensional

surfaces of constant segment density. The total fraction of segments enclosed by the surfaces is also reported in the legend. Clearly, the spherical segment distribution, characteristic of the isotropic structure of the equilibrium undeformed melt, assumes, upon imposition of the field α_{xx}, the shape of an ellipsoid of revolution with its long axis parallel to the *x*-coordinate axis. The segment density distribution of the C_{24} system shows a similar response upon imposition of the field to that displayed in Figure 11 for C_{78}.

The perturbation in chain shape seen in Figure 11 may result from two effects: (a) orientation of the segment clouds of individual polymer coils, such that their longest dimension becomes roughly parallel to the field direction; (b) distortion of the intrinsic shape of segment clouds, e.g., partial "unraveling" of the coils to form more elongated objects. To distinguish between these two effects, we analyzed separately the intrinsic shape of chains at different values of the field α_{xx}. A result from this analysis for the C_{78} system is shown in Figure 12. This figure presents the same information as Figure 11 above, the only difference being that the segment cloud of each individual chain was rotated such that *x*, *y*, and *z* coincided with the longest, intermediate, and shortest principal axis of its radius of gyration tensor, respectively, prior to averaging. In other words, the shape is analyzed not in the laboratory frame but in the frame of eigenvectors of the instantaneous radius of gyration tensor.[56] In this coordinate frame, the intrinsic overall shape of chains is seen to be that of a "cake of soap", as pointed out long ago for random walks by Šolc and Stockmayer[57] and subsequently seen[56] for RIS-based atomistically represented unperturbed chains. For the C_{78} system, a field as high as $\alpha_{xx} = 0.3$ has a negligible effect on the intrinsic shape of the chains: the shapes shown in Figure 12 for both $\alpha_{xx} = 0$ and $\alpha_{xx} = 0.3$ are practically identical, which indicates that, under the conditions considered in the present study, only *orientation* and not *distortion* of the segment clouds of chains is taking place in the C_{78} system.

This conclusion is further supported by Figure 13, which shows the effect of α_{xx} on the torsion angle distribution of chains. For the C_{78} system (Figure 13b) and α_{xx} values up to 0.30, the distribution of torsion angles remains very close to that of the undeformed melt, which, in turn, is indistinguishable from that of CUCs.[23,41] In the case of the shorter-chain C_{24} system, at the highest values of α_{xx} examined, the perturbation of the torsion angle distribution is no longer negligible; a significant shift from gauche to trans states is obvious in Figure 13a at $\alpha_{xx} = 0.75$. Under these conditions, one would expect that chains would not only be oriented but also be partially unraveled to intrinsically more elongated shapes. The intrinsic shapes of chains in the C_{24} system in the absence of field and in the presence of a strong field ($\alpha_{xx} = 0.75$) are compared directly in Figure 14. This is entirely analogous to Figure 12 but drawn at a higher value of the segment density. In the undeformed melt, the cloud again resembles a cake of soap. In the presence of the field, however, a distinctly different, more elongated cigarlike shape is obtained, indicative of the distortion of the intrinsic shape of the chains due to the field.

Stresses. Figures 15 and 16 show the magnitude of the stress tensor components developed in the two melts as a function of the imposed field α_{xx}. The open symbols in each figure represent the stress estimates based on

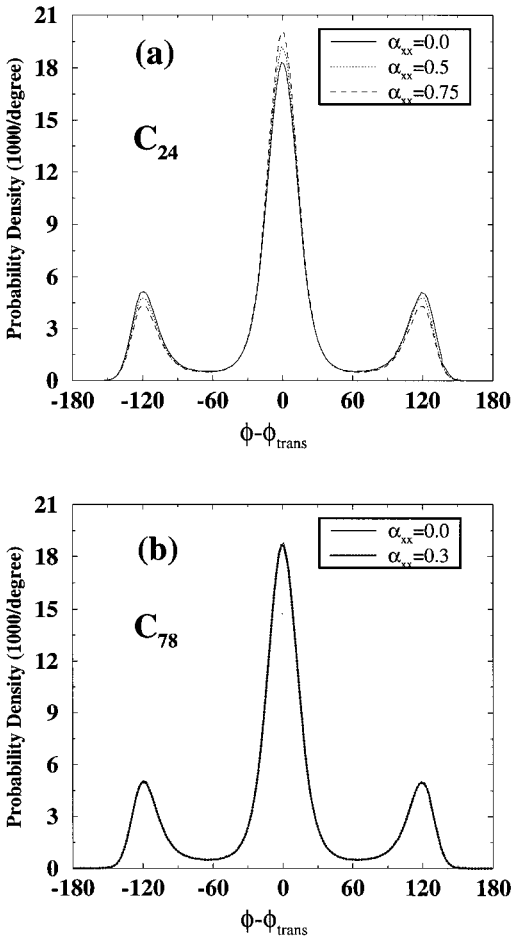

Figure 13. Torsion angle distribution for the C_{24} and C_{78} chain systems at various values of α_{xx} ($T = 450$ K, $b = 1$ atm).

b, α and $\tilde{\mathbf{c}}$ obtained from applying the affine model equation, eq 8, while the filled symbols represent the simulation results (obtained from applying the molecular virial theorem[58] on the strained configurations, with due consideration of the field forces exerted on chain ends). The virial theorem estimates are subject to much higher statistical uncertainty, owing to the fluctuations in instantaneous configuration. According to eq 8, τ_{xx} should increase with α_{xx} (following the increase of $\tilde{c}_{xx}$), τ_{yy} and τ_{zz} should remain constant, equal to $-b$, and all other (off-diagonal) components should be zero. Both figures support these predictions: as α_{xx} increases, τ_{xx} also increases in a nonlinear fashion, the increase being faster for the shorter C_{24} chain system. For example, for the same α_{xx} value, $\alpha_{xx} = 0.3$, $\tau_{xx} = 75$ atm for the C_{24} and $\tau_{xx} = 30$ atm for the C_{78} chain system. The figures further show that the agreement between the virial theorem-based results and the results from eq 8 is excellent, particularly at higher fields, for which the error bars on the virial stress results are significantly smaller compared to the absolute value of the stress. This confirms the utility of eq 8 for the stress tensor.

The nonlinear increase of τ_{xx} with α_{xx} is not a new observation in polymer dynamics. Rheological models used widely for the estimation of the elongational viscosity of polymer solutions and melts, such as the upper-convected Maxwell and the FENE models, predict a faster than linear increase of τ_{xx} with the elongational rate $\dot{\epsilon}_{xx}$. A direct comparison of the predictions of these models with our work would be interesting but requires

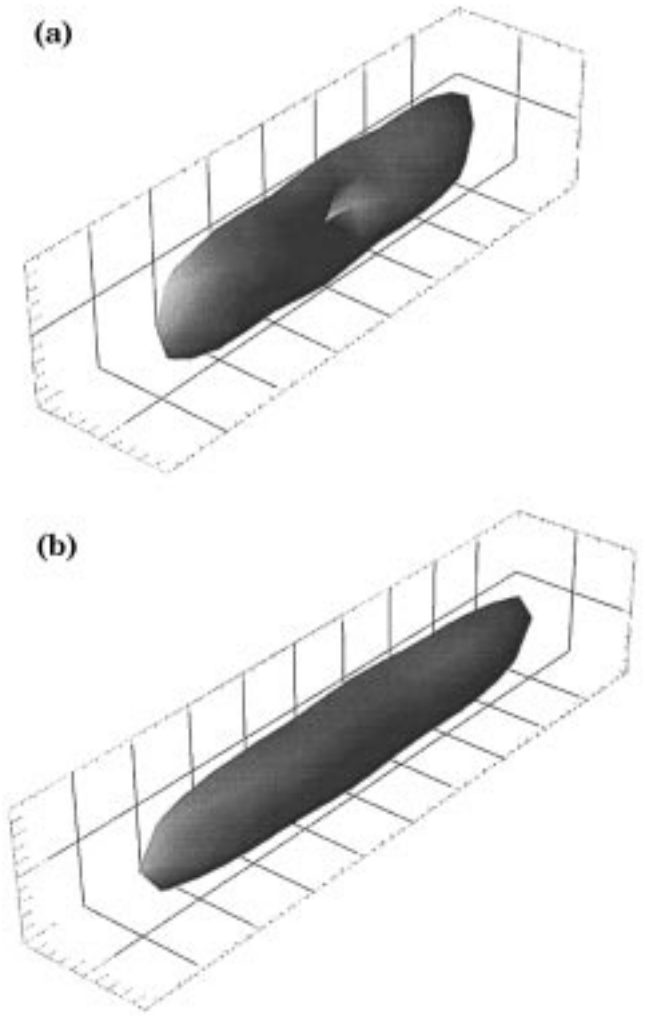

Figure 14. Same as Figure 12, but for the C_{24} system: (a) undeformed ($\alpha_{xx} = 0.0$) and (b) uniaxially stretched ($\alpha_{xx} = 0.75$) chains. The surfaces are drawn for a segment density equal to 40.0 mers/nm^3, and contain 28.3% and 47.7% of the total segments, respectively ($T = 450$ K, $b = 1$ atm). The distance between successive grid lines on the axes of the figure represents 7.5 Å of real length.

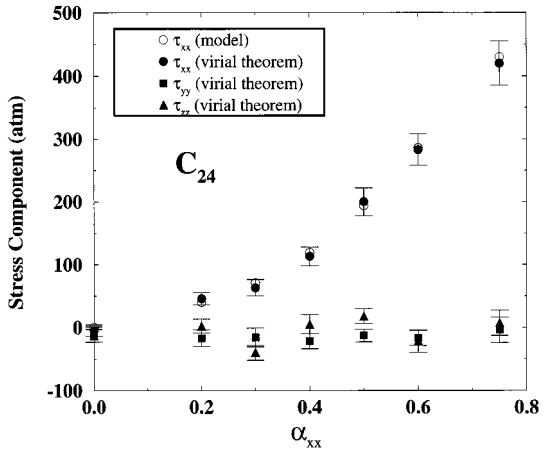

Figure 15. Stress tensor components in the C_{24} polymer melt as a function of the orienting field α_{xx} ($T = 450$ K, $b = 1$ atm). The open circles represent the predictions for τ_{xx} based on eq 8, whereas the filled symbols represent the predictions of the molecular virial theorem applied on the strained configurations. The statistical uncertainty in the open symbols is commensurate with the size of the symbols.

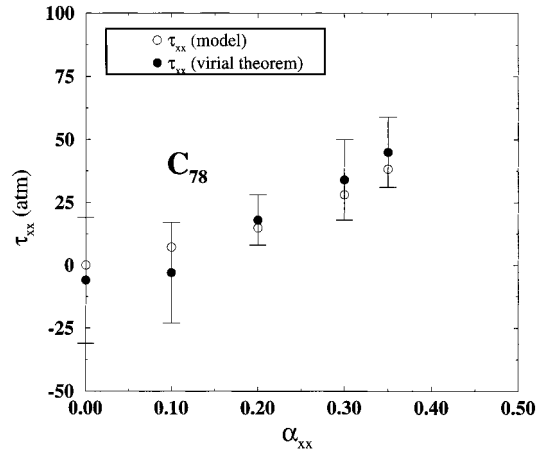

Figure 16. τ_{xx} component of the stress tensor in the C_{78} polymer melt as a function of the orienting field α_{xx} ($T = 450$ K, $b = 1$ atm). The open circles represent the predictions of eq 8, whereas the filled circles represent the predictions of the molecular virial theorem applied to the strained configurations. The statistical uncertainty in the open circles is commensurate with the size of the symbols.

a quantitative relation between α_{xx} and $\dot{\epsilon}_{xx}$. As discussed in section 3, the field α_{xx} considered in the present study is strictly a thermodynamic variable and can be related to the elongational strain rate only if an evolution equation is invoked either for the stress tensor or for the conformation tensor. Deriving such an evolution equation from molecular-level information is conceivable but has not been an objective of the present study. Thus, writing down a rigorous relation between α_{xx} and $\dot{\epsilon}_{xx}$ is not possible strictly on the basis of this simulation work alone. Alternatively, however, one can consider particular rheological models based on coarse-grained molecular pictures and derive the relation between α_{xx} and $\dot{\epsilon}_{xx}$ corresponding to these models.

For example, in the case of an extensional flow along the x-direction, the upper convected Maxwell model, corresponding to a picture of noninteracting Hookean dumbbells, yields a τ_{xx} equal to [eq (13.4.33) in ref 20, Vol 2, p 75]:

$$\tau_{xx} = -b + 2\frac{N_A}{M}\rho k_B T \frac{\lambda\dot{\epsilon}_{xx}}{(1 - 2\lambda\dot{\epsilon}_{xx})} \qquad (42)$$

with λ the relaxation time of the Hookean dumbbells (equivalent to the longest relaxation time or Rouse time of a Gaussian chain). This, together with our eq 26 for the dependence of $\tilde{c}_{xx}$ on α_{xx} and our stress equation, eq 8, proves that, for this rheological model, $\alpha_{xx} \equiv \lambda\dot{\epsilon}_{xx}$. Therefore, the comparison between $\tilde{c}_{xx}(\alpha_{xx})$ relations based on our simulation results and on the Gaussian chain model, presented in Figure 8, can also be looked at as a comparison of the corresponding $\tau_{xx}(\dot{\epsilon}_{xx})$ predictions: At high elongation rates, the upper convected Maxwell model overestimates the stress, because it does not account for the finite extensibility of chains.

Establishing a relation between $\tilde{c}_{xx}$ and the elongational rate $\lambda\dot{\epsilon}_{xx}$ for other models is not always a straightforward task. An interesting case which can also be worked out is that of the FENE model. By resorting to the slow flow expansion limit for the polymer contribution to the fluid stress (eq (13.5−17) in ref 20, Vol 2, p 79, which is based on the so-called Giesekus expression for the polymer stress) one can show that, in this case, $\alpha_{xx} \equiv [B/(B + 5)]\lambda\dot{\epsilon}_{xx}$. Clearly as $B \rightarrow \infty$ the Gauss (Hookean dumbbell) result is recoverd.

Table 6. Various Components of the Average Potential Energy and the Field Energy for the C_{24} Chain System (in J/g) as Functions of the Orienting Field α_{xx} (T = 450 K and b = 1 atm)

α_{xx}	nonbonded intramolecular	nonbonded intermolecular	bending	torsional	field
0.00	−34.4 ± 0.2	−252.8 ± 1.0	120.0 ± 0.4	208.8 ± 0.6	0.00
0.20	−33.0 ± 0.2	−253.8 ± 0.6	120.5 ± 0.4	207.8 ± 0.8	2.9 ± 0.1
0.30	−33.6 ± 0.2	−253.7 ± 0.6	121.1 ± 0.4	208.4 ± 0.6	5.2 ± 0.2
0.40	−33.2 ± 0.3	−255.4 ± 0.6	120.6 ± 0.5	207.0 ± 0.8	8.5 ± 0.2
0.50	−32.7 ± 0.2	−259.8 ± 1.3	120.0 ± 0.3	203.9 ± 0.7	13.3 ± 0.6
0.60	−32.0 ± 0.2	−261.7 ± 1.1	119.8 ± 0.3	202.3 ± 0.6	20.0 ± 0.5
0.75	−31.3 ± 0.2	−266.0 ± 0.7	119.4 ± 0.4	199.0 ± 0.8	30.7 ± 1.2

Table 7. Various Components of the Average Potential Energy and the Field Energy for the C_{78} Chain System (in J/g) as Functions of the Orienting Field α_{xx} (T = 450 K and b = 1 atm)

α_{xx}	nonbonded intramolecular	nonbonded intermolecular	bending	torsional	field
0.00	−45.4 ± 0.4	−275.5 ± 0.3	129.2 ± 0.2	229.4 ± 0.3	0.00
0.10	−45.3 ± 0.4	−275.5 ± 0.4	129.2 ± 0.2	229.5 ± 0.4	0.42 ± 0.02
0.20	−45.4 ± 0.5	−275.5 ± 0.4	129.0 ± 0.3	229.3 ± 0.3	1.02 ± 0.06
0.30[a]	−45.4 ± 0.4	−275.6 ± 0.4	129.1 ± 0.2	229.5 ± 0.3	1.90 ± 0.10
0.35[a]	−45.2 ± 0.4	−275.6 ± 0.3	129.1 ± 0.2	229.2 ± 0.4	2.60 ± 0.15

[a] Results obtained from simulations in the "superbox".

Free Energy of the Oriented Melt. In the special case of extensional flow, considered in these calculations (only $\alpha_{xx} \neq 0$), eqs 19 and 20 assume the forms

$$\frac{\Delta\tilde{G}}{N} \equiv \frac{\tilde{G}(T,b,\boldsymbol{\alpha}) - \tilde{G}_0(T,b,\mathbf{0})}{N} = -k_B T \int_0^{\alpha_{xx}} \tilde{c}_{xx}\, d\alpha_{xx} \quad (43)$$

$$\frac{\Delta A}{N} \equiv \frac{A(T,\rho,\tilde{\mathbf{c}}) - A_0(T,\rho,\mathbf{I})}{N} = \frac{\Delta\tilde{G}}{N} - b\frac{M}{N_A}\left(\frac{1}{\rho} - \frac{1}{\rho_0}\right) + k_B T \alpha_{xx} c_{xx} \quad (44)$$

The free energy differences $\Delta\tilde{G}/N$ and $\Delta A/N$ can therefore be calculated by a simple numerical integration of the function $\tilde{c}_{xx} = \tilde{c}_{xx}(\alpha_{xx})$ accumulated during the simulation runs for various α_{xx} values and shown in Figures 7−10. As usual, $\Delta A/N$ can be decomposed into an energetic and an entropic part:

$$\frac{\Delta A}{N} \equiv \frac{\Delta U}{N} - \frac{T\Delta S}{N} \quad (45)$$

The energetic component can be independently calculated as the change in ensemble-averaged total potential energy of the melt (configurational internal energy), directly from the simulation. Equations 43−45, therefore, permit calculating not only the Helmholtz free energy but also the entropy of the deformed melt relative to the undeformed state. Results for the two systems studied in the present work are shown in Figures 17 and 18. Figure 17 shows the effect of α_{xx} on the Helmholtz free energy components for the C_{24}, and Figure 18 shows that for the C_{78} chain system. The individual contributions making up the internal energy, and the field energy $k_B T \alpha_{xx} \tilde{c}_{xx}$, are shown in Tables 6 and 7, in units of Joules per gram of melt.

Figure 17 and Table 6 show that for very small values of α_{xx}, up to 0.2, the internal energy of the C_{24} melt remains unchanged; entropy, on the other hand, shows a small decrease. As α_{xx} increases to higher values (from 0.2 to about 0.4), both components show appreciable changes and contribute almost equally (with opposite signs) to the change in the free energy of the melt. For even higher field values (between 0.4 and 0.75), the reduction in internal energy becomes really large, but still smaller than the entropic contribution. As can be seen in Table 6, this large decrease in internal energy is a direct consequence of (a) the tendency of chains to assume more elongated intrinsic shapes (enhancement of trans conformational states, lowering of torsional energy, rise in nonbonded intramolecular energy) and (b) the enhanced lateral attractive interactions developing between the oriented chains (lowering

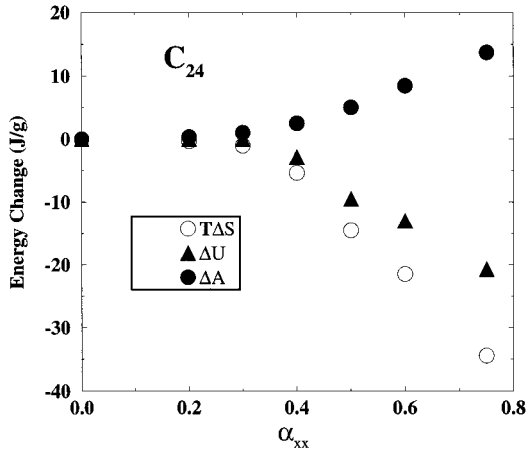

Figure 17. Change in Helmholtz free energy ΔA, internal energy ΔU, and entropy of deformation multiplied by the temperature $T\Delta S$ (all in units of J/g) relative to the equilibrium undeformed (α_{xx} = 0.0) state for the C_{24} polymer melt as a function of the field α_{xx} (T = 450 K, b = 1 atm).

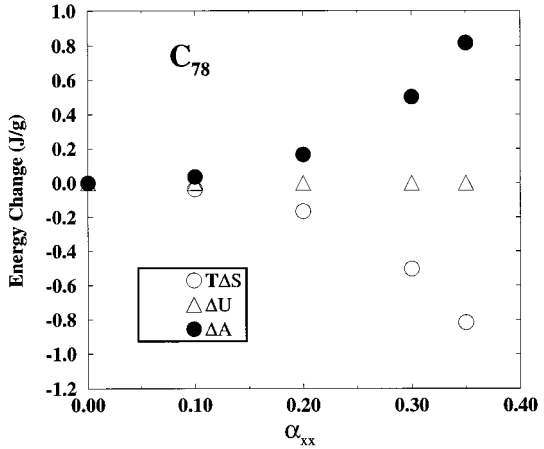

Figure 18. Change in Helmholtz free energy ΔA, internal energy ΔU, and entropy of deformation multiplied by the temperature $T\Delta S$ (all in units of J/g) relative to the equilibrium undeformed (α_{xx} = 0.0) state for the C_{78} polymer melt as a function of the field α_{xx} (T = 450 K, b = 1 atm).

of nonbonded intermolecular energy). It is these favorable lateral intermolecular interactions that cause the melt chains to assume more anisotropic shapes than CUCs subjected to the same field (compare Figure 7 and associated discussion). Table 6 shows that the decrease in the nonbonded intermolecular energy is somewhat larger than the torsional energy decrease for all α_{xx} values considered in the present study. Furthermore, the extension of chains brings about a small increase in nonbonded intramolecular energy. The net result is that intermolecular contributions to the energetic response are more significant than intrachain contributions. For example, at $\alpha_{xx} = 0.5$, the change in torsional energy is about -5 J/g, the change in nonbonded intramolecular energy is about $+2$ J/g, and the change in nonbonded intermolecular energy is about -7 J/g, while for $\alpha_{xx} = 0.75$ the corresponding numbers are ≈ -10, $+3$, and -13 J/g, respectively (see Table 6).

Figure 18 presents the corresponding picture for the longer C_{78} chain system. For this system, the range of field values where the entropic contribution continues to prevail is considerably more extended than in the shorter C_{24} melt. For all α_{xx} values studied in the present work (up to 0.35), no significant change in the internal energy is seen in the C_{78} system, and the response of the melt to the imposed field is purely entropic in character. Of course, a decline of the internal energy similar to the one observed in the C_{24} chain system should definitely be observed also for this system at higher α_{xx} values. However, it is interesting to point out that our work, by calculating the free energy and internal energy of deformation of the oriented C_{78} melt, has explicitly demonstrated that, in the range of low extension rates most relevant to applications, the response of a long-chain melt is purely entropic and no significant energetic changes take place. Our study has also shown that very small molecular weight analogues subjected to flows of the same Deborah number do not necessarily provide a reliable picture of the rheological response of a melt (compare Figures 17 and 18, Tables 6 and 7 under the same α_{xx} values). This should be borne in mind in future atomistic studies of melt dynamics.

The predominantly elastic response of polymer melts to an externally imposed field (in the small field regime) is in sharp contrast with the deformation in a glassy polymer, where the response is mainly energetic.[6] On the other hand, the emergence of an energetic (as opposed to entropic) response of the melt to deformation at high field strengths is a very important result of the present work, because it shows that the common practice of modeling the chains as independent "entropy springs" is not adequate at very large deformation rates. As seen in Figure 18, however, the assumption of a purely entropic response, underlying most rheological modeling, is satisfactory in the regime of long chains and low orienting fields, encountered in most real-life processing operations.

Melt Structure. Additional insight into the structural changes induced by the orienting field α_{xx} can be gained by studying the segment intermolecular and the chain center-of-mass pair distribution functions in directions parallel and perpendicular to the direction of the imposed field. The first is shown in Figure 19, and the second, in Figures 20 and 21. The corresponding functions in the isotropic, unoriented melt are also shown in the same figures, for comparison. According

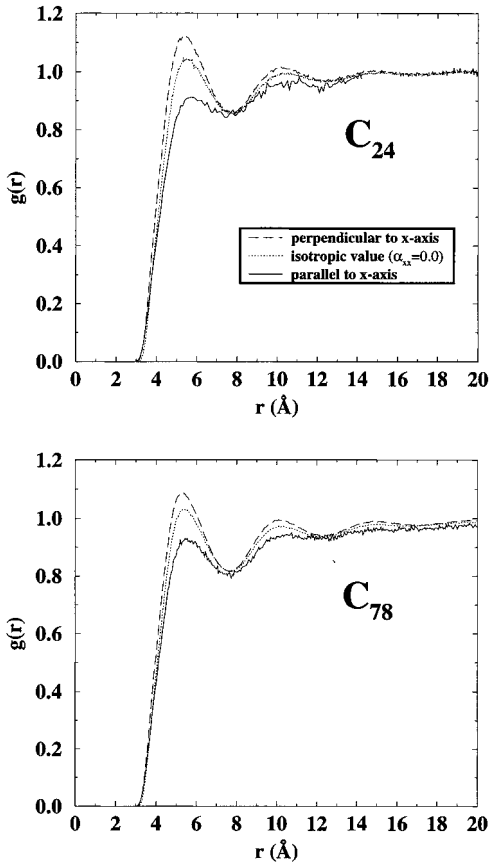

Figure 19. Intermolecular mer−mer pair distribution function along the directions perpendicular and parallel to the orienting field for the C_{24} (top) and the C_{78} (bottom) system, for $\alpha_{xx} = 0.3$. For comparison, the isotropic curve obtained in the absence of the field ($\alpha_{xx} = 0.0$) is also shown ($T = 450$ K, $b = 1$ atm).

to Figure 19, the imposition of α_{xx} causes a noticeable increase of intermolecular neighbors in directions perpendicular to the field relative to the isotropic case, and a corresponding decrease in the direction parallel to the field. The larger noise in this latter curve is due to poor sampling size along the *x*-direction (a cylindrical region of diameter 1 Å centered on the reference mer with its axis parallel to *x* was used for this purpose). The curve parallel to the field has been accumulated only up to a distance equal to half the box size, as opposed to the curve perpendicular to the field and the one corresponding to the isotropic melt, where the calculation was extended up to the box semidiagonal.[59] Differences between the directions parallel and perpendicular to the field are somewhat greater in the C_{24} case than in the C_{78} case. Another noteworthy feature of Figure 19 is that the peak corresponding to the first shell of intermolecular neighbors shifts to somewhat shorter distances in oriented melts perpendicular to the field and to somewhat longer distances in oriented melts parallel to the field, relative to the isotropic case. All these features are direct manifestations of the induced orientation of chains in the *x*-direction, which causes more and somewhat closer intermolecular contacts in the transverse (*y* and *z*) directions.

Figure 20 shows the effect of α_{xx} on the chain center-of-mass pair distribution function $g_{CM}(r)$. Results are rather noisy, due to the relatively small number of chains present. The first, important point to notice in the $g_{CM}(r)$ of the equilibrium unstrained melt is the

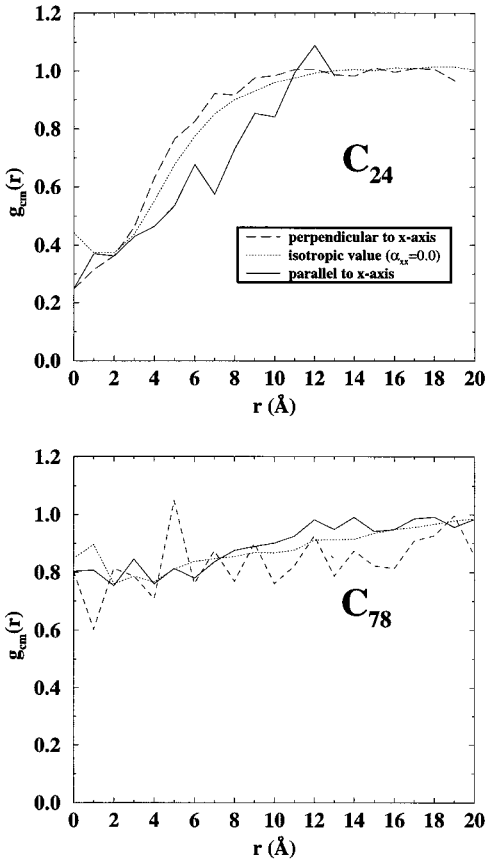

Figure 20. Chain center-of-mass pair distribution function in the directions perpendicular and parallel to the orienting field for the C_{24} (top) and the C_{78} (bottom) system, for $\alpha_{xx} = 0.3$. For comparison, the isotropic curve obtained in the absence of the field ($\alpha_{xx} = 0.0$) is also shown ($T = 450$ K, $b = 1$ atm).

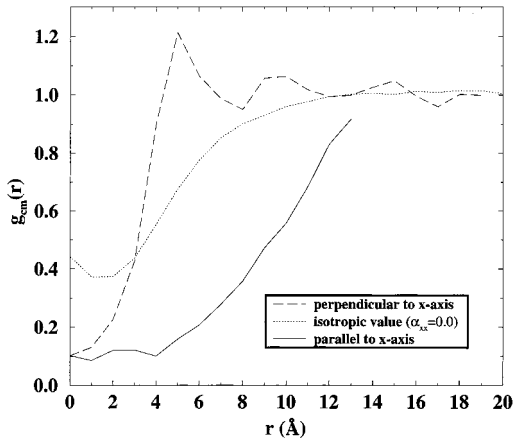

Figure 21. Chain center-of-mass pair distribution function in the directions perpendicular and parallel to the orienting field for the C_{24} system, for $\alpha_{xx} = 0.75$. For comparison, the isotropic curve in the absence of the field ($\alpha_{xx} = 0.0$) is also shown ($T = 450$ K, $b = 1$ atm).

absence of strong correlations between the centers of mass; in contrast to the intermolecular pair distribution function of mers, $g_{CM}(r)$ seems to exhibit no particular structure. Only a "correlation hole" region of radius commensurate with the chain radius of gyration is observed, wherein $g_{CM}(r)$ is significantly smaller than 1. The "depth" of the correlation hole in $g_{CM}(r)$ is larger for the short-chain system. Interestingly, $g_{CM}(0)$ assumes a nonzero value. This, although strange at first glance, is due to the fact that different chains can interpenetrate, their centers of mass coming very close without violating the nonoverlap requirement for mers. The application of an orienting field α_{xx} shifts $g_{CM}(r)$ upward in the direction perpendicular to the field and downward in the direction parallel to the field in the correlation hole region. This reflects a tendency of chains to "pack" with their longest dimension parallel to the orienting field (compare above discussion of chain shapes). All these effects are much stronger in the C_{24} system than in the long-chain C_{78} system.

Sharper structural correlations develop in the short-chain system at high enough values of α_{xx}. This is shown in Figure 21, obtained from the C_{24} chains for $\alpha_{xx} = 0.75$. In this case, $g_{CM}(r)$ in the direction perpendicular to the field is seen to display a shallow undulation, reminiscent of that seen in the intermolecular $g(r)$: very few neighbors are found at short (less than about 3 Å) distances, a peak develops at a distance around 5 Å, and a minimum is also observed at a distance of approximately 8 Å, followed by a hint of a second coordination shell at approximately 10 Å. On the contrary, the component of the distribution parallel to the field direction shows an extended area of exclusion; it exhibits no peak, increasing monotonically to the bulk value. This structure, developing in the short-chain systems for sufficiently high field values, is somewhat reminiscent of nematic order; it is facilitated by the strongly anisotropic shapes adopted by the melt chains (compare Figure 14).

7. Conclusions

In this work, we have presented the first step of a new, hierarchical methodology for the prediction of viscoelastic properties of polymer melts from the molecular constitution of chains through atomistic simulation. The present work has focused on the modeling of melt elasticity. Our analysis has made use of the conformation tensor $\tilde{\mathbf{c}}$, a coarse-grained descriptor of the overall polymer melt conformation, and of its conjugate "orienting field" $\boldsymbol{\alpha}$. Equilibration of the long-chain configurations at all length scales was made possible with the end-bridging Monte Carlo algorithm. Using these tools, we have been able to calculate from an atomistic model, for the first time, the dependence of the Helmholtz energy of an oriented polymer melt and of its energetic and entropic components on the degree of molecular orientation. Two polymer melt systems have been investigated, of average chain lengths C_{24} and C_{78} and polydispersity index 1.09. The bulk simulation results have further been compared with results obtained from (a) continuous unperturbed chains subjected to the same orienting fields; and (b) theoretical models, such as the Gaussian, the freely-jointed chain, and the FENE model.

Generally, the overall chain conformation that develops in response to an orienting field and, therefore, the functional dependence of the free energy on orientation differ between the atomistic melt simulation and the simpler models. For the Gaussian model (Figure 8), this is because of its failure to account for the finite extensibility of chains. Freely-jointed chain and FENE models reproduce the response of long-chain melts, but their response is less anisotropic than that of the melt for the short-chain system (C_{24}) subjected to very high fields ($\alpha_{xx} > 0.4$) (Figures 9 and 10). Single, atomistically detailed uperturbed chains respond to the field less

anisotropically than melt chains, the difference between the two responses becoming dramatic for short chains at high fields (Figure 7). The latter difference was shown to be due to the development of favorable lateral intermolecular interactions between oriented chains in the melt. In other words, the melt response to deformation is not purely entropic, but has a significant energetic component at high fields. The elongation of chain shapes induced by the orienting field and the associated energetic response to deformation were shown to be more expressed for short chains, which have fewer internal degrees of freedom to accommodate the deformation.

Our work further demonstrated that only very high values of the imposed orienting field can lead to substantial distortion of chain shapes. For most values of α_{xx} investigated in this work, a mere reorientation but no significant distortion of the intrinsic shape of the chain segment cloud was observed. It was only for high values $\alpha_{xx} > 0.40$ in the short-chain C_{24} system that a quantitative deviation from the instantaneous unperturbed shape of chains could be observed. Having an atomistic simulation procedure at our disposal that can simply orient long chains in the melt without deforming their shapes is a significant accomplishment, for it ensures that the response of the system to the external field is linear. From the rheological point of view, the behavior of the system is expected to fall within the limits of the Newtonian plateau. Our MC procedure for generating oriented melts is thus a very attractive alternative to NEMD simulations, wherein ensuring a satisfactory signal-to-noise ratio within the limits of available computer time dictates the use of relatively short chains and extremely high deformation rates, which exceed by many orders of magnitude the rates encountered in usual polymer processing operations.

The stress in the oriented melt has been obtained through the virial theorem and found to be consistent with an expression cast in terms of $\tilde{\mathbf{c}}$ and the fields b and $\boldsymbol{\alpha}$, which postulates an affine deformation of chain ends (eq 8).

One should point out that our computational procedure of mapping out the melt free energy as a function of a coarse-grained descriptor of chain conformation (i.e., calculating the potential of mean force as a function of a small set of structural parameters) could be extended to other structural parameters than the conformation tensor. For example, a higher-dimensional $\tilde{\mathbf{c}}$, corresponding to the first two or three modes of the Rouse model, could be selected.[33] The melt free energy could be obtained as a function of the components of that $\tilde{\mathbf{c}}$ by introducing an appropriate number of conjugate field variables $\boldsymbol{\alpha}$ and conducting atomistic MC simulations at different values of $\boldsymbol{\alpha}$.

Currently, work is in progress to relax the equilibrated strained melt configurations by dynamic simulation and to examine the temporal evolution of ensemble-averaged quantities that are directly related to polymer conformation. By mapping the relaxation curves for these conformational properties onto theoretical expressions based on an appropriate coarse-grained model for the dynamics of polymer melts (e.g., Rouse model), one is able to extract the relaxation time spectrum of the melt and from that its zero-shear rate viscosity and shear relaxation modulus.

Acknowledgment. This work was supported by the European Commission through BRITE/EuRam Project BRPR-CT96-0145. Stimulating discussions with other project partners, and in particular with Professors Manuel Laso and Hans Christian Öttinger, are deeply appreciated. Also appreciated are vigorous exchanges of ideas with Dr. S. Lustig. We are grateful to the General Secretariat of Research and Technology of Greece for partial support in the form of a PENED 95 grant, No. 218. We are indebted to ICE/HT-FORTH for a generous allocation of time on the Origin 2000 machine.

A. Conformation Tensor

We show here that the assumption of affine deformation of chain ends leads to eq 7 relating the conformation tensor with the (macroscopic) deformation gradient tensor. To this end, we envision that, at a certain time, a homogeneous deformation is applied on the polymer that displaces chain ends affinely, in the sense that their positions are changed in the same way as material points in a macroscopic continuum description. Let $\mathbf{r}_0$ and $\mathbf{r}_N$ be the positions of the start and end points of a chain before the deformation and $\mathbf{r'}_0$ and $\mathbf{r'}_N$ the positions of the same points after the deformation. If $\mathbf{F}$ is the deformation gradient tensor, then

$$\mathbf{r'}_0 = \mathbf{F}\cdot\mathbf{r}_0 \tag{A.1}$$

and

$$\mathbf{r'}_N = \mathbf{F}\cdot\mathbf{r}_N \tag{A.2}$$

By subtracting eq A.1 from eq A.2, we get

$$\mathbf{R} = \mathbf{F}\cdot\mathbf{R}_0 \tag{A.3}$$

where $\mathbf{R}_0$ and $\mathbf{R}$ are the chain end-to-end vectors *before* and *after* the deformation, respectively. The conformation tensor $\tilde{\mathbf{c}}$, therefore, after the deformation is

$$\tilde{\mathbf{c}} \equiv 3\left\langle \frac{\mathbf{RR}}{\langle R^2\rangle_0}\right\rangle = 3\left\langle \frac{(\mathbf{F}\cdot\mathbf{R}_0)(\mathbf{F}\cdot\mathbf{R}_0)}{\langle R^2\rangle_0}\right\rangle \tag{A.4}$$

which in component form is also written as

$$\tilde{c}_{\alpha\beta} = 3\left\langle \frac{\sum_{\gamma=1}^{3}\sum_{\delta=1}^{3} F_{\alpha\gamma}R_{0\gamma}F_{\beta\delta}R_{0\delta}}{\langle R^2\rangle_0}\right\rangle \tag{A.5}$$

i.e.,

$$\tilde{c}_{\alpha\beta} = 3\sum_{\gamma=1}^{3}\sum_{\delta=1}^{3} F_{\alpha\gamma}F_{\beta\delta}\left\langle \frac{R_{0\gamma}R_{0\delta}}{\langle R^2\rangle_0}\right\rangle \tag{A.6}$$

i.e.,

$$\tilde{c}_{\alpha\beta} = \sum_{\gamma=1}^{3}\sum_{\delta=1}^{3} F_{\alpha\gamma}F_{\beta\delta}\tilde{c}_{\gamma\delta,0} \tag{A.7}$$

where $\tilde{\mathbf{c}}_0$ is the conformation tensor before the deformation. But $\tilde{\mathbf{c}}_0 \equiv \mathbf{I}$, the unit tensor, therefore,

$$\tilde{c}_{\alpha\beta} = \sum_{\gamma=1}^{3}\sum_{\delta=1}^{3} F_{\alpha\gamma}F_{\beta\delta}I_{\gamma\delta} \tag{A.8}$$

i.e.,

$$\tilde{c}_{\alpha\beta} = \sum_{\gamma=1}^{3} F_{\alpha\gamma} F_{\beta\gamma} \tag{A.9}$$

which in vector notation form gives

$$\tilde{\mathbf{c}} = \mathbf{F}\cdot\mathbf{F}^{\mathrm{T}} \qquad \text{QED} \tag{A.10}$$

B. Stress Tensor

We prove here eq 8 based on rational thermodynamics and the assumption of an affine deformation of chain ends. The starting point is eq 6, which in component form is written as

$$\tau_{\alpha\beta} = \frac{N_{\mathrm{A}}}{M}\rho \sum_{\gamma=1}^{3} F_{\alpha\gamma} \frac{\partial(A/N)}{\partial F_{\beta\gamma}} \tag{B.1}$$

A simplified notation will be adopted here, wherein all variables of a function, except that with respect to which partial differentiation takes place, are implied to be constant. Invoking the functional dependence, eq 3, postulated for A/N,

$$\begin{aligned}\tau_{\alpha\beta} &= \frac{N_{\mathrm{A}}}{M}\rho \sum_{\gamma=1}^{3} F_{\alpha\gamma}\left(\frac{\partial(A/N)}{\partial\rho}\frac{\partial\rho}{\partial F_{\beta\gamma}} + \sum_{\epsilon=1}^{3}\sum_{\zeta=1}^{3}\frac{\partial(A/N)}{\partial\tilde{c}_{\epsilon\zeta}}\frac{\partial\tilde{c}_{\epsilon\zeta}}{\partial F_{\beta\gamma}}\right)\\ &= -\rho\sum_{\gamma=1}^{3} F_{\alpha\gamma}\rho^2\frac{N_{\mathrm{A}}}{M}\frac{\partial(A/N)}{\partial\rho}\frac{\partial v}{\partial F_{\beta\gamma}} + \frac{N_{\mathrm{A}}}{M}\rho\sum_{\gamma=1}^{3}\sum_{\epsilon=1}^{3}\sum_{\zeta=1}^{3} F_{\alpha\gamma}\frac{\partial(A/N)}{\partial\tilde{c}_{\epsilon\zeta}}\frac{\partial\tilde{c}_{\epsilon\zeta}}{\partial F_{\beta\gamma}}\\ &= \tau_{1,\alpha\beta} + \tau_{2,\alpha\beta}\end{aligned} \tag{B.2}$$

with $v = 1/\rho$ being the specific volume of the polymer. In eq B.2, $\boldsymbol{\tau}_1$ is the part of $\boldsymbol{\tau}$ that depends on b and $\boldsymbol{\tau}_2$ is the part of $\boldsymbol{\tau}$ that depends on $\tilde{\mathbf{c}}$. To see this, we first calculate component $\tau_{1,\alpha\beta}$ by making use of the definition of b, eq 4:

$$\tau_{1,\alpha\beta} = -\rho\sum_{\gamma=1}^{3} F_{\alpha\gamma} b\frac{\partial v}{\partial F_{\beta\gamma}} = -b\rho\sum_{\gamma=1}^{3} F_{\alpha\gamma}\frac{\partial v}{\partial F_{\beta\gamma}} \tag{B.3}$$

To calculate the derivative $\partial v/\partial F_{\beta\gamma}$, we use $v = v_0 \det(\mathbf{F})$ and $\partial(\det\mathbf{F})/\partial F_{\beta\gamma} = \det(\mathbf{F})(F_{\beta\gamma}{}^{-1})^{\mathrm{T}}$. With these, eq B.3 becomes

$$\tau_{1,\alpha\beta} = -b\rho v\sum_{\gamma=1}^{3} F_{\alpha\gamma}F_{\gamma\beta}{}^{-1} \tag{B.4}$$

or

$$\tau_{1,\alpha\beta} = -bI_{\alpha\beta} \tag{B.5}$$

with $\mathbf{I}$ being the unit second-order tensor.

To calculate component $\boldsymbol{\tau}_2$, we first evaluate the derivative $\partial\tilde{c}_{\epsilon\xi}/\partial F_{\beta\gamma}$; this is done by using the relation $\tilde{\mathbf{c}} = \mathbf{F}\cdot\mathbf{F}^{\mathrm{T}}$ (eq 7 and Appendix A), which in component form reads

$$\tilde{c}_{\epsilon\zeta} = \sum_{\eta=1}^{3} F_{\epsilon\eta}F_{\zeta\eta} \tag{B.6}$$

Substituting eq B.3 into eq B.2 gives

$$\begin{aligned}\tau_{2,\alpha\beta} &= \frac{N_{\mathrm{A}}}{M}\rho\sum_{\gamma=1}^{3}\sum_{\epsilon=1}^{3}\sum_{\zeta=1}^{3} F_{\alpha\gamma}\frac{\partial(A/N)}{\partial\tilde{c}_{\epsilon\zeta}}\sum_{\eta=1}^{3}\left(\frac{\partial F_{\epsilon\eta}}{\partial F_{\beta\gamma}}F_{\zeta\eta} + F_{\epsilon\eta}\frac{\partial F_{\zeta\eta}}{\partial F_{\beta\gamma}}\right)\\ &= \frac{N_{\mathrm{A}}}{M}\rho\sum_{\gamma=1}^{3}\sum_{\epsilon=1}^{3}\sum_{\zeta=1}^{3}\sum_{\eta=1}^{3} F_{\alpha\gamma}\frac{\partial(A/N)}{\partial\tilde{c}_{\epsilon\zeta}}\left(\frac{\partial F_{\epsilon\eta}}{\partial F_{\beta\gamma}}F_{\zeta\eta} + F_{\epsilon\eta}\frac{\partial F_{\zeta\eta}}{\partial F_{\beta\gamma}}\right)\\ &= \frac{N_{\mathrm{A}}}{M}\rho\sum_{\gamma=1}^{3}\sum_{\epsilon=1}^{3}\sum_{\zeta=1}^{3}\sum_{\eta=1}^{3} F_{\alpha\gamma}\frac{\partial(A/N)}{\partial\tilde{c}_{\epsilon\zeta}}(\delta_{\epsilon\beta}\delta_{\eta\gamma}F_{\zeta\eta} + \delta_{\zeta\beta}\delta_{\eta\gamma}F_{\epsilon\eta})\\ &= \frac{N_{\mathrm{A}}}{M}\rho\left(\sum_{\gamma=1}^{3}\sum_{\zeta=1}^{3} F_{\alpha\gamma}\frac{\partial(A/N)}{\partial\tilde{c}_{\beta\zeta}}F_{\zeta\gamma} + \sum_{\gamma=1}^{3}\sum_{\epsilon=1}^{3} F_{\alpha\gamma}\frac{\partial(A/N)}{\partial\tilde{c}_{\epsilon\beta}}F_{\epsilon\gamma}\right)\\ &= \frac{N_{\mathrm{A}}}{M}\rho\sum_{\zeta=1}^{3}\frac{\partial(A/N)}{\partial\tilde{c}_{\beta\zeta}}\left(\sum_{\gamma=1}^{3} F_{\alpha\gamma}F_{\zeta\gamma}\right) + \frac{N_{\mathrm{A}}}{M}\rho\sum_{\epsilon=1}^{3}\frac{\partial(A/N)}{\partial\tilde{c}_{\epsilon\beta}}\left(\sum_{\gamma=1}^{3} F_{\alpha\gamma}F_{\epsilon\gamma}\right)\end{aligned} \tag{B.7}$$

which, with the use of eq B.6, gives

$$\tau_{2,\alpha\beta} = \frac{N_{\mathrm{A}}}{M}\rho\sum_{\zeta=1}^{3}\frac{\partial(A/N)}{\partial\tilde{c}_{\beta\zeta}}\tilde{c}_{\alpha\zeta} + \frac{N_{\mathrm{A}}}{M}\rho\sum_{\epsilon=1}^{3}\frac{\partial(A/N)}{\partial\tilde{c}_{\epsilon\beta}}\tilde{c}_{\alpha\epsilon} \tag{B.8}$$

Since the tensor $\tilde{\mathbf{c}}$ is symmetric,

$$\frac{\partial(A/N)}{\partial\tilde{c}_{\beta\zeta}} = \frac{\partial(A/N)}{\partial\tilde{c}_{\zeta\beta}} \tag{B.9}$$

which, using eq B.8, becomes

$$\tau_{2,\alpha\beta} = \frac{N_{\mathrm{A}}}{M}\rho\sum_{\zeta=1}^{3}\tilde{c}_{\alpha\zeta}\frac{\partial(A/N)}{\tilde{c}_{\zeta\beta}} + \frac{N_{\mathrm{A}}}{M}\rho\sum_{\epsilon=1}^{3}\tilde{c}_{\alpha\epsilon}\frac{\partial(A/N)}{\tilde{c}_{\epsilon\beta}} \tag{B.10}$$

i.e.,

$$\tau_{2,\alpha\beta} = 2\frac{N_{\mathrm{A}}}{M}\rho\sum_{\gamma=1}^{3}\tilde{c}_{\alpha\gamma}\frac{\partial(A/N)}{\partial\tilde{c}_{\gamma\beta}} \tag{B.11}$$

By substituting eqs B.5 and B.11 into eq B.2, we get

$$\tau_{\alpha\beta} = -bI_{\alpha\beta} + 2\frac{N_{\mathrm{A}}}{M}\rho\sum_{\gamma=1}^{3}\tilde{c}_{\alpha\gamma}\frac{\partial(A/N)}{\partial\tilde{c}_{\gamma\beta}} \tag{B.12}$$

which is exactly eq 8 reported in section 3.

c. Freely-Jointed Chain Model

According to Flory,[47] the distribution function for the chain end-to-end vector for a freely-jointed chain consisting of N_{K} bonds each of length b_{K} is written as

$$p_0(\mathbf{R}) = (2\pi^2\, R b_{\mathrm{K}}{}^2)^{-1}\, I_{N_{\mathrm{K}}}\left(\frac{R}{b_{\mathrm{K}}}\right) \tag{C.1}$$

where

$$I_{N_K}\left(\frac{R}{b_K}\right) = (\pi/4)N_K(N_K-1)\sum_{t=0}^{\tau}\left[\frac{(-1)^t}{t!(N_K-t)!}\right]\left[\frac{N_K-\frac{R}{b_K}-2t}{2}\right]^{N_K-2} \quad \text{(C.2)}$$

and τ is the integer satisfying

$$\frac{\left(N_K-\frac{R}{b_K}-2\right)}{2} \le \tau < \frac{\left(N_K-\frac{R}{b_K}\right)}{2} \quad \text{(C.3)}$$

In order to keep the limits of the outer integration in eq 32 of section 5 between 0 and 1, we introduce the scaled variable x through

$$x \equiv \frac{R}{N_K b_K} \quad \text{(C.4)}$$

Then, the function $f(x)$ appearing in section 5 is defined as

$$f_{N_K}(x) \equiv \frac{8}{\pi} I_{N_K}\left(\frac{R}{b_K}\right) \quad \text{(C.5)}$$

From eq C.1 and the definition (C.5), it is then straightforward to extract the expressions for the function $f_{N_K}(x)$ used in eq 32 of section 5:

•for $N_K = 1$

$$f_1(x) = 4\,\delta(x-1) \qquad 0 \le x < 1 \quad \text{(C.6)}$$

with δ the Dirac delta function.

•for $N_K = 2$

$$f_2(x) = 2 \qquad 0 \le x < 1 \quad \text{(C.7)}$$

•for $N_K = 3$

$$f_3(x) = \begin{cases} 6x & 0 \le x < \frac{1}{3} \\ 3-3x & \frac{1}{3} \le x < 1 \end{cases} \quad \text{(C.8)}$$

•for $N_K = 4$

$$f_4(x) = \begin{cases} \frac{(4-4x)^2-4(2-4x)^2}{4} & 0 \le x < \frac{1}{2} \\ \frac{(4-4x)^2}{4} & \frac{1}{2} \le x < 1 \end{cases} \quad \text{(C.9)}$$

•for $N_K = 5$

$$f_5(x) = \begin{cases} \frac{(5-5x)^3-5(3-5x)^3+10(1-5x)^3}{24} & 0 \le x < \frac{1}{5} \\ \frac{(5-5x)^3-5(3-5x)^3}{24} & \frac{1}{5} \le x < \frac{3}{5} \\ \frac{(5-5x)^3}{24} & \frac{3}{5} \le x < 1 \end{cases} \quad \text{(C.10)}$$

•for $N_K = 6$

$$f_6(x) = \begin{cases} \frac{(6-6x)^4-6(4-6x)^4+15(2-6x)^4}{192} & 0 \le x < \frac{1}{3} \\ \frac{(6-6x)^3-6(4-6x)^4}{192} & \frac{1}{3} \le x < \frac{2}{3} \\ \frac{(6-6x)^4}{192} & \frac{2}{3} \le x < 1 \end{cases} \quad \text{(C.11)}$$

References and Notes

(1) Allen, M. P.; Tildesley, D. J. *Computer Simulation of Liquids*; Oxford University Press: Oxford, U.K., 1987.
(2) Roe, R.-J., Ed. *Computer Simulation of Polymers*; Prentice Hall: Englewood Cliffs, NJ, 1991.
(3) Colbourn, E. A., Ed. *Computer Simulation of Polymers*; Longman: Essex, U.K., 1994.
(4) Monnerie, L. M., Suter, U. W., Eds. *Atomistic Modeling of Physical Properties*; *Advances in Polymer Science* 116; Springer-Verlag: Berlin 1994.
(5) Theodorou, D. N.; Suter, U. W. *Macromolecules* **1985**, *18*, 1467.
(6) Theodorou, D. N.; Suter, U. W. *Macromolecules* **1986**, *19*, 139.
(7) Gusev, A. A.; Suter, U. W. *J. Chem. Phys.* **1993**, *99*, 2228.
(8) Greenfield, M. L.; Theodorou, D. N. *Mol. Simul.* **1997**, *19*, 329.
(9) Rapold, R. F.; Suter, U. W.; Theodorou, D. N. *Macromol. Theory Simul.* **1994**, *3*, 19.
(10) Smith, G. D.; Yoon, D. Y. *J. Chem. Phys.* **1994**, *100*, 649. Paul, W.; Yoon, D. Y.; Smith, G. D. *J. Chem. Phys.* **1995**, *103*, 1702.
(11) Baljon, R. C.; Grest, G. S.; Witten, T. A. *Macromolecules* **1995**, *28*, 1835.
(12) Mondell, M.; Grest, G. S. *J. Chem. Phys.* **1995**, *103*, 7156.
(13) Han, J.; Gee, R.; Boyd, R. H. *Macromolecules* **1994**, *27*, 7781. Jin, Y.; Pernice, M.; Boyd, R. H. *Comput. Theor. Polym. Sci.* **1996**, *6*, 9.
(14) Xu, Z.; de Pablo, J. J.; Kim, S. *J. Chem. Phys.* **1995**, *102*, 5836. Xu, Z. F.; Khare, R.; de Pablo, J. J.; Kim, S. *J. Chem. Phys.* **1997**, *106*, 9858.
(15) Keunings, R. In *Fundamentals of Computer Modeling for Polymer Processing*; Tucker, C. L., III, Ed. Carl Hansen Verlag: New York, 1989; p 402.
(16) Denn, M. M. *Annu. Rev. Fluid Mech.* **1990**, *22*, 13.
(17) Moldenaers, P., Keunings, R., Eds. *Theoretical and Applied Rheology*; Proceedings of the XIth International Congress on Rheology; Brussels, Elsevier: Amsterdam, 1992.
(18) Doi, M.; Edwards, S. F. *The Theory of Polymer Dynamics*; Clarendon: Oxford, U.K., 1986.
(19) Curtiss, C. F.; Bird, R. B. *J. Chem. Phys.* **1981**, *74*, 2016, 2026.
(20) Bird, R. B.; Armstrong, R. C.; Hassager, O.; Curtiss, C. F. *Dynamics of Polymeric Liquids*, Fluid Mechanics (Vol. 1) and Kinetic Theory (Vol. 2); Wiley: New York, 1987.
(21) Öttinger, H. C. *Stochastic Processes in Polymeric Fluids*; Springer Verlag: Berlin, 1995.
(22) Molenaar, J.; Koopmans, R. J. *J. Rheol.* **1994**, *38*, 99. Koopmans, R. J. *Polym. Eng. Sci.* **1992**, *32*, 1741, 1750, 1755.
(23) Pant, P. V. K.; Theodorou, D. N. *Macromolecules* **1995**, *28*, 7224.
(24) Mark, J. E.; Erman, B. *Rubberlike Elasticity: A Molecular Primer*; John Wiley: New York, 1988.
(25) Flory, P. J. *Principles of Polymer Chemistry*; Cornell University Press: Ithaca, NY, 1953.
(26) Treloar, L. R. G. *The Physics of Rubber Elasticity*, 3rd ed.; Clarendon: Oxford, U.K., 1975.
(27) Eichinger, B. E. *Annu. Rev. Phys. Chem.* **1983**, *34*, 359.
(28) Lodge, A. S. *Trans. Faraday Soc.* **1956**, *52*, 120.
(29) Wagner, M. H. *Rheol. Acta* **1979**, *18*, 33.
(30) Dzyaloshinskii, I. E.; Volovick, G. E. *Ann. Phys.* **1980**, *125*, 67.
(31) Grmela, M. *Physica* **1986**, *21D*, 179.
(32) Grmela, M. *Phys. Lett. A* **1988**, *130*, 81.
(33) Beris, A. N.; Edwards, B. J. *Thermodynamics of Flowing Systems With Internal Microstructure*; Oxford University Press: Oxford, U.K., 1994.
(34) Mavrantzas, V. G.; Beris, A. N. *J. Chem. Phys.* submitted for publication.
(35) Mavrantzas, V. G. Surface Effects on the Structure and Rheology of Polymer Solutions. Ph.D. Thesis, University of Delaware, Newark, DE, 1994.

(36) Lustig, S. R.; Shay, R. M.; Caruthers, J. M. *J. Rheol.* **1996**, *40*, 69.
(37) Weiner, J. H. *Statistical Mechanics of Elasticity*; Wiley: New York, 1983.
(38) Tanner, R. I. *Engineering Rheology*; Clarendon: Oxford, U.K., 1985.
(39) Astarita, G.; Marrucci, G. *Principles of Non-Newtonian Fluid Mechanics*; McGraw Hill: London, 1974.
(40) Chandler, D. *Introduction to Modern Statistical Mechanics*; Oxford University Press: New York, 1987.
(41) Dodd, L. R.; Theodorou, D. N. *Adv. Polym. Sci.* **1994**, *116*, 249.
(42) Van der Ploeg, P.; Berendsen, H. J. C. *J. Chem. Phys.* **1982**, *76*, 3271.
(43) Smit, B.; Karaborni, S.; Siepmann, J. I. *J. Chem. Phys.* **1995**, *102*, 2126.
(44) Ryckaert, J. P.; Bellemans, A. *Chem. Phys. Lett.* **1975**, *30*, 123.
(45) Frenkel, D.; Smit, B. *Understanding Molecular Simulation: From Algorithms to Applications*; Academic Press: New York, 1996.
(46) Boone, T. D. *Prediction of Glass-Melt Behavior and Penetrant Sorption in Vinyl Polymers via Molecular Simulations*; Ph.D. Thesis, University of California, Berkeley, 1995.
(47) Flory, P. J. *Statistical Mechanics of Chain Molecules*; Interscience: New York, 1969.
(48) de Pablo, J.J.; Laso, M.; Suter, U. W. *J. Chem. Phys.* **1992**, *96*, 2395.
(49) Spyriouni, T.; Economou, I. G.; Theodorou, D. N. *Macromolecules* **1997**, *30*, 4744.
(50) Smith, G. D.; Yoon, D. Y.; Jaffe, R. L.; Colby, R. H.; Krishnamoorti, R.; Fetters, L. J. *Macromolecules* **1996**, *29*, 3462.
(51) Mattice, W. L.; Suter, U. W. *Conformational Theory of Large Molecules*; Wiley: New York, 1994.
(52) Horton, J.C.; Squires, G.L.; Boothroyd, A.T.; Fetters, L.J.; Rennie, R.J.; Glinka, C.J.; Robinson, R.A. *Macromolecules* **1989**, *22*, 681.
(53) Fetters, L.J.; Graessley, W.W.; Krishnamoorti, R.; Lohse, D.J. *Macromolecules* **1997**, *30*, 4973.
(54) Paul, W.; Smith, G.D.; Yoon, D.Y. *Macromolecules* **1997**, *30*, 7772.
(55) Han, J.; Jaffe, R.L.; Yoon, D.Y. *Macromolecules* **1997**, *30*, 7245.
(56) Theodorou, D. N.; Suter, U. W. *Macromolecules* **1985**, *18*, 1206.
(57) Šolc, K.; Stockmayer, W. H. *J. Chem. Phys.* **1971**, *54*, 2756.
(58) Theodorou, D.N.; Dodd, L.R.; Boone, T.D.; Mansfield, K.F. *Makromol. Chem., Theory Simul.* **1993**, *2*, 191.
(59) Theodorou, D. N.; Suter, U. W. *J. Chem. Phys.* **1985**, *82*, 955.

MA9714878